A deep X-ray view of the bare AGN Ark 120. I. Revealing the Soft X-ray Line Emission

J. N. Reeves[1,2], D. Porquet[3], V. Braito[1,4], E. Nardini[2], A. Lobban[5], T. J. Turner[6]

ABSTRACT

The Seyfert 1 galaxy, Ark 120, is a prototype example of the so-called class of bare nucleus AGN, whereby there is no known evidence for the presence of ionized gas along the direct line of sight. Here deep (> 400 ks exposure), high resolution X-ray spectroscopy of Ark 120 is presented, from *XMM-Newton* observations which were carried out in March 2014, together with simultaneous *Chandra*/HETG exposures. The high resolution spectra confirmed the lack of intrinsic absorbing gas associated with Ark 120, with the only X-ray absorption present originating from the ISM of our own Galaxy, with a possible slight enhancement of the Oxygen abundance required with respect to the expected ISM values in the Solar neighbourhood. However, the presence of several soft X-ray emission lines are revealed for the first time in the *XMM-Newton* RGS spectrum, associated to the AGN and arising from the He and H-like ions of N, O, Ne and Mg. The He-like line profiles of N, O and Ne appear velocity broadened, with typical FWHM widths of ~ 5000 km s^{-1}, whereas the H-like profiles are unresolved. From the clean measurement of the He-like triplets, we deduce that the broad lines arise from gas of density $n_{\rm e} \sim 10^{11}$ cm^{-3}, while the photoionization calculations infer that the emitting gas covers at least 10% of 4π steradian. Thus the broad soft X-ray profiles appear coincident with an X-ray component of the optical–UV Broad Line Region on sub-pc scales, whereas the narrow profiles originate on larger pc scales, perhaps coincident with the AGN Narrow Line Region. The observations show that Ark 120 is not intrinsically bare and substantial X-ray emitting gas exists out of our direct line of sight towards this AGN.

Subject headings: galaxies:active — Seyferts: individual: Ark 120 — X-rays: galaxies

[1]Center for Space Science and Technology, University of Maryland Baltimore County, 1000 Hilltop Circle, Baltimore, MD 21250, USA: jreeves@umbc.edu

[2]Astrophysics Group, School of Physical and Geographical Sciences, Keele University, Keele, Staffordshire, ST5 5BG, UK; j.n.reeves@keele.ac.uk

[3]Observatoire Astronomique de Strasbourg, Université de Strasbourg, CNRS, UMR 7550, 11 rue de l'Université, F-67000 Strasbourg, France

[4]INAF - Osservatorio Astronomico di Brera, Via Bianchi 46 I-23807 Merate (LC), Italy

[5]Dept of Physics and Astronomy, University of Leicester, University Road, Leicester LE1 7RH, UK

[6]Department of Physics, University of Maryland Baltimore County, 1000 Hilltop Circle, Baltimore, MD 21250, USA

1. Introduction

Photo-ionised or "warm" absorbers are commonly observed in at least 50% of the UV/X-ray spectra of Seyfert 1s and type-1 QSO and are an important constituent of AGN (Reynolds 1997, Crenshaw, Kraemer & George 2003, Porquet et al. 2004, Blustin et al. 2005, McKernan et al. 2007, Turner & Miller 2009). Indeed the Seyfert warm absorbers that are frequently observed at high spectral resolution with *XMM-Newton* and *Chandra* are now known to give rise to numerous narrow absorption lines, usually blue-shifted – implying outflowing winds – of a few hundred $\mathrm{km\,s^{-1}}$ up to a few thousand $\mathrm{km\,s^{-1}}$. These arise from various elements over a wide range of ionisation levels and column densities, especially from iron, oxygen, carbon, nitrogen, neon, silicon and sulfur (Kaastra et al. 2000, Kaspi et al., 2002, McKernan et al. 2003, Blustin et al. 2003). Signatures range from the lowly ionised Unresolved Transition Array (UTA) of M-shell iron ($<$ Fe XVII) at $\sim 16 - 17\mathrm{\AA}$ (Sako et al. 2001, Behar et al. 2001), to absorption from highly ionised (H-like and He-like) iron which may originate from an accretion disk wind (Reeves et al. 2004, Risaliti et al. 2005a, Braito et al. 2007, Turner et al., 2008, Tombesi et al. 2010, Gofford et al. 2013). These spectroscopic measurements can reveal crucial information on the outflow kinematics, physical conditions and locations relative to the central continuum source – ranging from the inner nucleus (0.01 pc) to the galactic disk or halo (10 kpc).

However a small class of nearby Seyfert galaxies exist which show no (or very little) X-ray or UV absorption. These AGN are the so-called *"bare nucleus"* Seyferts or bare AGN. In principle the lack of intrinsic absorbing gas in these bare AGN allows a clean measurement of the innermost regions of the AGN and of the central engine closest to the black hole, removing any uncertainties as to how the absorbing gas is modeled. Ark 120 (or Arakelian 120) is a nearby ($z = 0.032713$, Osterbrock & Phillips 1977, Theureau et al. 2005) and X-ray bright ($F_{0.5-10\,\mathrm{keV}} = 5.3 \times 10^{-11}\,\mathrm{erg\,cm^{-2}\,s^{-1}}$, $F_{14-195\,\mathrm{keV}} = 7.0 \times 10^{-11}\,\mathrm{erg\,cm^{-2}\,s^{-1}}$; Patrick et al. 2011, Baumgartner et al. 2013) bare nucleus Seyfert 1. Along with its sister AGN, Fairall 9 (Emmanoulopoulos et al. 2011, Lohfink et al. 2012), it is the prototype example of a bare AGN. Indeed it is one of the brightest and cleanest bare AGN known, displaying neither intrinsic reddening in its IR/optical continuum nor evidence for absorption in UV and X-rays (Crenshaw et al. 1999, Reynolds 1997), allowing a clear view of the innermost regions of the AGN. A further key advantage for studying Ark 120 is that it has a well determined reverberation based black hole mass, of $M_{\mathrm{BH}}{=}1.5{\times}10^8\,\mathrm{M_\odot}$ (Peterson et al. 2004).

An open question is whether Ark 120 is intrinsically bare and devoid of circumnuclear X-ray emitting and/or absorbing gas, which may pose a challenge for unified schemes of AGN that imply the existence of wide scale obscuring and emitting gas (Antonucci 1993). Indeed, Vaughan et al. (2004) presented an initial 100 ks *XMM-Newton* observation of Ark 120 in 2003, which from the spectra obtained with the RGS (Reflection Grating Spectrometer, den Herder et al. 2001) showed no significant soft X-ray emission or absorption features associated to the AGN. Furthermore the X-ray continuum was found to be smooth from the soft X-ray band up to 10 keV, with a large but featureless soft X-ray excess present at energies below 2 keV. This was also confirmed in a *Suzaku* study by Nardini et al. (2011), who favored a relativistic accretion disk reflection origin for the soft X-ray excess and broad iron Kα line. In an alternative explanation for the broad band spectrum, Tatum et al. (2012) accounted for the iron Kα emission through Compton scattering off an accretion disk wind, which had to be viewed out of the direct line of sight in this AGN. Most recently, Matt et al. (2014) presented a simultaneous ~ 100 ks *XMM-Newton* and *NuSTAR* observation

of Ark 120 obtained in 2013 and showed that the bare broad-band X-ray spectrum could be explained by Comptonization of UV photons through a warm scattering medium associated to an accretion disk corona.

This paper is the first of a series of papers to report upon the analysis of an unprecedented deep observational campaign on Ark 120, which was subsequently obtained with *XMM-Newton* in 2014, with a total exposure exceeding 400 ks (PI, D. Porquet). Part of the long *XMM-Newton* observations were performed simultaneously with *NuSTAR* to provide broad band hard X-ray coverage and with the High Energy Transmission Grating (HETG, Canizares et al. 2005) on-board *Chandra* to provide a high resolution view of the iron K band region. Here we concentrate on the high signal to noise and high resolution soft X-ray spectrum obtained with the RGS spectrometer on-board *XMM-Newton*. The primary goal is to determine whether the soft X-ray spectrum of Ark 120 is intrinsically bare and devoid of circumnuclear X-ray gas, or indeed whether there are any signatures of ionized emission or absorption, which could arise from the accretion disk, the AGN broad and narrow line regions or from a nuclear outflow. We also present a search for any soft X-ray emission lines at high resolution from the Chandra/HETG above 1 keV from Mg, Si, S. Subsequent papers will report in detail on the modeling of the iron Kα line profile obtained as part of these observations (paper II, Nardini et al. 2016), as well as the nature of the broad band UV to hard X-ray continuum of Ark 120 (paper III, Porquet et al. 2016, in preparation).

The paper is organized as follows. In Section 2, we describe the analysis of the RGS observations, while in Section 3 the overall properties of the soft X-ray RGS spectrum are presented. Section 4 is devoted to the analysis of the Galactic ISM absorption towards Ark 120 and the subsequent modeling of the soft X-ray continuum. Section 5 then describes the first detection of soft X-ray emission lines from Ark 120 that have now been made possible through the deep RGS exposure and Section 6 discusses their potential origin in the broad and narrow lined regions from the AGN. Values of $H_0 = 70\,\mathrm{km\,s^{-1}\,Mpc^{-1}}$, and $\Omega_{\Lambda_0} = 0.73$ are assumed throughout and errors are quoted at 90% confidence ($\Delta\chi^2 = 2.7$), for 1 parameter of interest. All spectral parameters are quoted in the rest-frame of the AGN, at $z = 0.032713$, unless otherwise stated. A conversion between energy and wavelength of $E = (12.3984\,\text{Å}/\lambda)\,\mathrm{keV}$ is adopted throughout.

2. Observations and Data Reduction

2.1. XMM-Newton Observations of Ark 120

XMM-Newton observed Ark 120 four times between 18-24 March 2014, over 4 consecutive satellite orbits. Each observation was approximately 130 ks in total duration, with the details of all four observations listed in Table 1. First order dispersed spectra were obtained with the RGS and were reduced using the RGSPROC script as part of the XMM-Newton SAS software v14.0. After screening the data for periods of high background, the net exposures for each RGS spectrum varied between $102.8 - 116.6$ ks (see Table 1). Prior to spectral analysis, channels due to bad pixels on the RGS CCDs were ignored as well as the two malfunctioning CCDs for RGS 1 and RGS 2 respectively. This yielded net background subtracted count rates of between $0.653\pm0.003\,\mathrm{s^{-1}} - 0.795\pm0.003\,\mathrm{s^{-1}}$ for RGS 1 and $0.746\pm0.003\,\mathrm{s^{-1}} - 0.909\pm0.003\,\mathrm{s^{-1}}$ for RGS 2, with the brightest observation being the first one in the series of four consecutive XMM-Newton

orbits. In each case, the background count rate represented less than 5% of the total count rate and thus the RGS observations were dominated by the AGN.

Spectra from the RGS 1 and RGS 2 were then also combined into a single RGS 1+2 spectrum for each of the four XMM-Newton sequences, having checked that the resultant spectra were consistent with each other before and after combining the two RGS modules. Note that the spectral response files were subsequently averaged over the effective areas of the two RGS modules. In order to provide a very simplistic parameterization of the RGS spectra, we fitted the 0.35–2.0 keV energy range (or 6.20Å– 35.4Å) with a continuum comprising a powerlaw plus blackbody component, whereby the blackbody emission provides an initial zeroth order description of the known soft excess towards this AGN (Vaughan et al. 2004, Nardini et al. 2011, Matt et al. 2014). An initial Galactic absorption of hydrogen column density of $N_{\rm H} = 9.8 \times 10^{20}\,{\rm cm}^{-2}$ (Kalberla et al. 2005) was adopted, modeled with the "Tuebingen–Boulder" absorption model (hereafter TBABS in XSPEC) using the cross–sections and Solar ISM abundances of Wilms et al. (2000).

Figure 1 shows the combined RGS 1+2 spectra for each of the 4 sequences, whereby the spectral parameters are all consistent within the margin of error; the average photon index was found to be $\Gamma = 2.09\pm0.04$, a blackbody temperature of $kT = 132 \pm 4$ eV and a neutral absorbing column in the local ($z = 0$) Galactic frame of $N_{\rm H} = (8.3 \pm 0.3) \times 10^{20}\,{\rm cm}^{-2}$, slightly lower compared to the expected Galactic neutral H I column from 21 cm measurements above. Nonetheless the fit is statistically poor, with a reduced chi-squared of $\chi^2/{\rm dof} = 3197.2/2308 = 1.385$ (where dof is the number of degrees of freedom in the fit), with strong residuals around the position of the neutral O I edge as well as systematic-like residuals throughout the spectrum. However it can be seen that all 4 sequences are consistent with each other, aside from some small differences in their absolute fluxes, with the brightest spectrum corresponding to the first *XMM-Newton* observation (0.4–2.0 keV band flux, $F_{0.4-2.0\,{\rm keV}} = 3.31 \pm 0.02 \times 10^{-11}\,{\rm erg\,cm}^{-2}\,{\rm s}^{-1}$) and the faintest corresponding to the 2nd and 4th observations as above ($F_{0.4-2.0\,{\rm keV}} = 2.72\pm0.02 \times 10^{-11}\,{\rm erg\,cm}^{-2}\,{\rm s}^{-1}$).

As the four spectra are consistent in shape, aside from a small difference in absolute flux of $\pm10\%$ between the observations, they were subsequently combined to produce a single, deep, high signal to noise RGS spectrum of Ark 120. This yielded net source count rates of $0.705 \pm 0.001\,{\rm s}^{-1}$ and $0.808 \pm 0.001\,{\rm s}^{-1}$ for each of the combined RGS 1 and RGS 2 spectra, with net exposures of 431.9 ks and 430.8 ks respectively. Note the total number of source counts over all four sequences, obtained from combining both of the RGS 1+2 modules, is $> 6.5 \times 10^5$ counts, with an effective total exposure of 862.7 ks providing a very high S/N soft X-ray spectrum of Ark 120. The subsequent combined spectrum was binned into $\Delta\lambda = 0.03$ Å bins, which over-samples the RGS spectral resolution by at least a factor of $\sim \times 2$ compared to the FWHM resolution. Due to the high count rate statistics, χ^2 minimization was employed in the subsequent spectral fitting, as typically there are ~ 700 counts per 0.03Å resolution bin, corresponding to a S/N of > 25 per bin.

2.2. Chandra HETG Observations of Ark 120

The High Energy Transmission Grating (HETG) onboard *Chandra* also observed Ark 120 from 17 March to 22 March 2014. Due to scheduling constraints, the *Chandra* observations were split into 3 se-

quences, overlapping with the 1st, 2nd and 3rd of the *XMM-Newton* sequences, with the 2nd sequence shorter than the other two, see Table 1 for details. Spectra were extracted with the CIAO package v4.3. Only the first order dispersed spectra were considered for both the MEG (Medium Energy Grating) and HEG (High Energy Grating) and the ± 1 orders for each grating were subsequently combined for each sequence. No significant spectral variability was observed between the 3 sequences and the spectra were consistent, with only modest $\sim 10\%$ variations in source flux. Therefore the spectra were combined from all three sequences to yield a single 1st order spectrum for each of the MEG and HEG, yielding respective net source count rates of $0.868 \pm 0.003\,\mathrm{s}^{-1}$ and $0.491 \pm 0.002\,\mathrm{s}^{-1}$ respectively for a total exposure time of 120.5 ks. Thus the total counts obtained exceeded 1.0×10^5 and 5×10^4 counts for MEG and HEG respectively. Note that the background contribution towards the count rate was negligible. Due to the high flux ($7 \times 10^{-11}\,\mathrm{erg\,cm}^{-2}\,\mathrm{s}^{-1}$ from 0.5-10 keV) and high count rates obtained from Ark 120, the zeroth order image and spectra were not usable due to severe pile-up of the central source.

The resultant 2014 1st order source spectra were subsequently binned to $\Delta\lambda = 0.01\,\text{Å}$ and $\Delta\lambda = 0.005\,\text{Å}$ bins for MEG and HEG respectively, which over-samples their respective FWHM spectral resolutions by a factor of $\times 2$. The C-statistic was employed in the subsequent spectral fits with the HETG, as although the overall count rate is high, towards the lower energy (longer wavelength) end of each grating spectrum the total source counts per bin drops below $N < 20$ in some bins. In the case of χ^2 minimization, this would lead to the continuum level being somewhat underestimated at soft X-ray energies.

3. The Soft X-ray Spectrum of Ark 120

Initially we concentrated on the analysis of the time-averaged 2014 *XMM-Newton* RGS observations. Figure 2 shows the overall 2014 νF_ν RGS spectrum of Ark 120, fluxed against a powerlaw of $\Gamma = 2$ in the soft X-ray band. The spectrum shown in Figure 2 is largely devoid of any strong ionized absorption lines in the AGN rest frame, as might be expected for Ark 120 given its past record as a bare Seyfert 1 galaxy and the lack of any warm absorber in the AGN (e.g. Vaughan et al. 2004). The expected rest frame positions of several $1s - 2p$ resonance lines (e.g from the He and H-like ions of N, O, Ne and Mg) are marked in the figure and there appears to be no significant absorption lines at any of these positions. However in the local ($z = 0$) observed frame, there appears to be several absorption features, in particular around the position of the neutral O I edge at $\sim 23\,\text{Å}$ there is a strong resonance absorption line (at 23.5Å or 527 eV) which may be identified with the Kα absorption line due to O I in our galaxy (Gorczyca et al. 2013). In addition another strong absorption line is observed near 31.2Å, which likewise may be attributed to the neutral Kα resonance line of N. Thus it appears clear we need to account for the absorption in the ISM due to our own galaxy in the soft X-ray spectrum of Ark 120, which we investigate below. Furthermore, although there appears little in the way of intrinsic ionized absorption towards Ark 120, there may be some indication ionized X-ray *emission* lines associated with the AGN, for instance associated with O VII, O VIII, Ne IX or Mg XII.

4. X-ray Absorption in the Galactic ISM towards Ark 120

Before investigating the presence of any ionized gas in emission (or absorption) intrinsic to Ark 120, we first attempt to model the absorption associated with the line of sight through the ISM of our own Galaxy. Due to the relatively low Galactic latitude of Ark 120 ($b = -21°.1$), the Galactic H I column is thought to be relatively high, with $N_H = 9.78 \times 10^{20}$ cm^{-2} as measured from 21 cm surveys (Stark et al. 1992, Kalberla et al. 2005) and thus this absorption needs to be modeled before we can accurately determine the intrinsic emission properties of the AGN. The Galactic hydrogen column was allowed to vary, noting that there can also be an additional contribution associated with molecular hydrogen (e.g. Willingale et al. 2013)

We fitted the combined mean 2014 RGS spectrum, adopting a powerlaw plus blackbody form to parameterize the soft X-ray continuum of Ark 120. As the RGS bandpass contains a contribution from both the hard X-ray powerlaw extending up to higher energies up to at least 70 keV (e.g. Matt et al. 2014, Porquet et al. 2016), as well as the prominent soft excess below 2 keV, we adopt both components in order to account for any spectral curvature present in the soft X-ray band. The AGN continuum emission was parameterized by a photon index of $\Gamma = 2.15 \pm 0.05$ and a blackbody temperature of $kT = 110 \pm 10$ eV. For the Galactic absorption, we initially adopted the TBVARABS model of Wilms et al. (2000), which accounts for the photoelectric absorption edges due to abundant elements in the X-ray band and allows for the possibility of variable abundances compared to chosen tabulated Solar values. A neutral hydrogen column of $N_H = (9.4 \pm 0.4) \times 10^{20}$ cm^{-2} was found, close to the reported 21 cm value above, with a relative O abundance compared to those in Wilms et al. (2000) or Asplund et al. (2009) of $A_0 = 1.39 \pm 0.10$.

However while this model provides a reasonable first order parameterization of the soft X-ray continuum of Ark 120, the fit is statistically very poor, with a reduced χ^2 corresponding to $\chi^2_\nu = \chi^2/\mathrm{dof} = 1561.3/938$. The TBVARABS or TBABS models only include the bound–free photoelectric absorption associated with the K and L-shell edges of abundant elements, but do not include any resonance absorption line structure due to the neutral ionization states of these elements. For instance Figure 3 (upper panel) shows the fluxed RGS spectrum (obtained against a simple unabsorbed $\Gamma = 2$ powerlaw model) around the neutral O edge region, with the above TBVARABS photoelectric absorption model super-imposed upon the spectrum. It is apparent that the prominent O I Kα absorption line observed near 23.5 Å (or 527 eV) is left unmodelled, whilst in reality the drop in the spectrum around the O edge (observed between 22.7Å–23.0Å) is not sharp, which is likely due to the presence of several resonances around the edge threshold energy (see de Vries et al. 2003, Gorczyca et al. 2013, Gatuzz et al. 2014). Indeed if we parameterize the 23.5 Å absorption with a simple narrow ($\sigma = 1$ eV) Gaussian absorption line we obtain an observed frame line energy of 527.2 ± 0.2 eV (or $\lambda = 23.52 \pm 0.01$ Å), which is in very good agreement with the expected energy of 527.4 eV, as also found from measurements towards Galactic binary systems (Gatuzz et al. 2014). Furthermore a second strong absorption line is present at $E = 396.6 \pm 0.5$ eV or 31.26 ± 0.04 Å (e.g. see Figure 2, lowest panel), which is in agreement with the expected position of the N I Kα line at 396.1 eV (Kaastra et al. 2011). The parameters of these Galactic absorption lines are also listed in Table 2. Upon addition of both of these ad-hoc Galactic absorption lines, the fit statistic to the RGS data improves to $\chi^2_\nu = 1392.7/934$, although the model is still formally rejected by the data.

4.1. A Comparison between ISM Absorption Models

A more physical model was then adopted to model the Galactic ISM absorption towards Ark 120, using the TBNEW model, which is an improved higher resolution version of the original TBABS or TBVARABS ISM absorption model of Wilms et al. (2000). The TBNEW model includes the various resonance absorption lines around the positions of the neutral O K-shell, Ne K-shell and Fe L-shell edges[1]. The ISM abundance table of Wilms et al. (2000) was also adopted for the modeling. The power-law plus blackbody continuum form was retained from before, although the parameters are allowed to vary freely. The goodness of fit obtained is subsequently improved compared to the simpler TBVARABS model ($\chi^2_\nu = 1344.0/936$) and the model is able to self consistently account for the strong O I Kα absorption line present observed at 527.2 eV (or $\lambda = 23.52$Å) in the $z = 0$ frame. Figure 3 (lower panel) also shows a zoom-in around the O K-shell region, but with the best-fit TBNEW overlaid on the fluxed RGS spectrum. In addition to the O I Kα absorption line, the model provides a better description of the data around the O K-shell edge, due to the various higher order resonance line structures, which produces a more gradual decrease at the position of the O K-shell edge. Figure 4 displays the same model, but now folded through the RGS instrumental response, versus the count rate spectrum and it can be seen that the model reproduces both the O I Kα edge region.

We note here that the excess emission blue-wards of the O K-shell edge region is likely associated with emission from the O VII triplet, in the region from 561 eV to 574 eV in the AGN rest frame, as can be seen in Figure 4. Indeed several ionized emission lines are observed from the AGN in the RGS spectrum, predominantly from the He and H like ions for N, O, Ne and Mg and the fit statistic improves considerably upon their inclusion in the model to $\chi^2_\nu = 1087.3/914$. The soft X-ray emission line properties of Ark 120 are discussed in detail in Section 5.

In addition the TBNEW model also self consistently models the absorption around the neutral Fe L and Ne K edges respectively, for instance some structure around the Fe L edge is also visible at 17.5Å (but much weaker than at Oxygen) in the fluxed spectrum in Figure 2. However the absorption line structure is not included around the N I K-shell edge region in TBNEW and therefore we retain the simple Gaussian absorption line to parameterize the visible N I Kα absorption line at 396.6 eV. We subsequently adopt the TBNEW model of the Galactic absorption as our initial baseline model for the ISM absorption towards Ark 120, with the baseline absorption and continuum (powerlaw plus blackbody) parameters listed in Table 2. Note that while the O I Kα absorption line is self consistently fitted in the TBNEW model, the simple Gaussian line parameterization obtained from before is listed also in Table 2 for completeness.

Overall the hydrogen column density obtained by the TBNEW model is $N_{\mathrm{H}} = (8.8 \pm 0.4) \times 10^{20}$ cm^{-2}, which is slightly below the reported 21 cm value of $N_{\mathrm{H}} = 9.78 \times 10^{20}$ cm^{-2}. However the neutral Oxygen abundance relative to the ISM values collated in Wilms et al. (2000) or Asplund et al. (2009) (of O/H $= 4.90 \times 10^{-4}$) is left free to vary (other elements are fixed at Solar). With respect to this value, the O abundance along the line of sight in the Galactic ISM is found to be mildly super-Solar, with $A_{\mathrm{O}} = 1.62 \pm 0.10$. If instead we adopt the earlier photospheric Solar abundance table of Grevesse & Sauval (1998), which

---

[1] see http://pulsar.sternwarte.uni-erlangen.de/wilms/research/tbabs/ for further details of the TBNEW model.

has a higher absolute oxygen abundance (of $O/H = 6.76 \times 10^{-4}$), then the relative O abundance compared to this value is lower ($A_O = 1.17 \pm 0.08$), while the hydrogen column is consistent with the previous value ($N_H = 9.0 \pm 0.4 \times 10^{20}$ cm^{-2}).

We then compared the Ark 120 soft X-ray spectrum with the ISMABS absorption model (Gatuzz et al. 2014). In addition to the updated resonance line cross-sections around the O, Ne K-shell and Fe L-shell complexes, the model also can include the contribution from ISM absorption from once and twice ionized ions from most of the cosmically abundant elements, as has been observed towards both Galactic sources and AGN (Pinto et al. 2010, 2012). A further advantage of the ISMABS model is that it allows the user to directly determine the column density of both the neutral atoms of abundant elements (as well as the ionized species), which can also be inferred indirectly from the TBNEW model from the hydrogen column and then relative abundance ratio.

Applying the ISMABS absorption model to the Ark 120 RGS spectrum results in a very similar fit as per the TBNEW model (with $\chi^2_\nu = 1086.6/911$) and the comparison of the parameters between these two ISM models are tabulated in Table 3. The hydrogen column density along the line of sight through our galaxy is also similar, with $N_H = (8.5 \pm 0.4) \times 10^{20}$ cm^{-2}. The neutral O column density was also allowed to vary, which primarily contributes towards the O I Kα absorption line as well as the higher order absorption, as per the TBNEW model. The neutral O column density is found to be $N_O = (6.5 \pm 0.3) \times 10^{17}$ cm^{-2}, which thus corresponds to an abundance ratio of $O/H = (7.7 \pm 0.5) \times 10^{-4}$, which is a factor of $A_O = 1.57 \pm 0.10$ above the relative O/H abundance value tabulated in Wilms et al. (2000), although again it is consistent with the higher O abundances tabulated by Anders & Grevesse (1989) and Grevesse & Sauval (1998).

The column densities of neutral N, Ne and Fe were also allowed to vary, the best fit values obtained from the ISMABS model are:- $N_N = (7.2 \pm 2.7) \times 10^{16}$ cm^{-2}, $N_{Ne} = (1.2 \pm 0.3) \times 10^{17}$ cm^{-2} and $N_{Fe} = (2.6 \pm 0.6) \times 10^{16}$ cm^{-2} respectively. (see Table 3). Note the N/H and Fe/H abundances are consistent with the Solar values in Wilms et al. (2000), as tabulated in Table 3, while the Ne/H abundance appears slightly higher compared to these tabulated values. All other elemental column densities were fixed according to their default Solar abundances in the ISMABS model, which otherwise assumes values calculated from Grevesse & Sauval (1998)[2], for a given hydrogen column.

Finally there appears to be no evidence for any ionized absorption associated with the Galactic ISM towards Ark 120. If for the ISMABS model we allow the column densities of once ionized O (denoted O$^+$) and twice ionized O (denoted O^{2+}) to vary (at $z = 0$), then only upper limits are found corresponding to $N_{O+} < 4.2 \times 10^{16}$ cm^{-2} and $N_{O^{2+}} < 0.6 \times 10^{16}$ cm^{-2}. These limits are at least a factor of $\times 10$ and $\times 100$ smaller respectively than the neutral O column through our Galaxy. Neither is there any evidence for any ISM absorption associated with the host galaxy of Ark 120, in the rest frame at $z = 0.032713$. The limit on the column of any neutral O absorption at $z = 0.032713$ is $N_O < 2.5 \times 10^{16}$ cm^{-2}, which translates into a hydrogen column of $N_H < 5 \times 10^{19}$ cm^{-2} assuming a Solar abundance of $O/H = 4.9 \times 10^{-4}$ according to Wilms et al. (2000). This is perhaps not surprising upon inspection of the RGS data; at a redshift of

---

[2]Note that ISMABS also assumes that the He abundance is 10% of that of hydrogen

$z = 0.032713$, the O I Kα absorption line at 527.2 eV (or 23.52Å) corresponds to an observed energy of 510.5 eV (or 24.29Å) and there is subsequently no evidence for absorption at these positions in either Figure 3 or 4.

4.2. Dependence on the Soft X-ray Continuum

The above analysis suggests that at least the Oxygen abundance (and possibly Ne) in the Galactic ISM towards Ark 120 could be somewhat higher than some of the tabulated Solar ISM values (Wilms et al. 2000, Lodders 2003, Asplund et al. 2009). However while the column densities of O, Ne and Fe are well determined from the discrete atomic features (absorption lines and edges) in the RGS spectrum, the absolute hydrogen column density is inferred from the downwards curvature of the spectrum towards the lowest energies. Thus the measured N_H values may depend on how the soft X-ray continuum is modeled. Therefore instead of the simple powerlaw plus blackbody continuum form, a continuum consisting of a powerlaw (responsible for the continuum above 2 keV) and a Comptonized disk blackbody spectrum was adopted, parameterized in this case by the COMPTT model (Sunyaev & Titarchuk 1985, Titarchuk 1994). The latter component represents the Compton upscattered Wien tail of the optically-thick inner disk emission, which may be produced by a warm scattering layer above the disk and it has been suggested that such an emission component could reproduce the mainly featureless UV to soft X-ray excesses observed in many AGN (Done et al. 2012, Jin et al. 2012). The main effect on the spectrum is that this produces a broader soft excess than a single unmodified blackbody component, as the latter would peak only in the UV band.

Upon adopting instead COMPTT form for the soft X-ray excess, it is found that the hydrogen column density was somewhat higher compared to the powerlaw plus blackbody case. The absorption parameters are tabulated in Table 3 and applied to both the TBNEW and ISMABS absorption models (denoted as TBNEW2 and ISMABS2 respectively in Table 3). It can be seen that the neutral hydrogen column has increased for both cases, e.g. for the TBNEW case, then $N_H = (11.1 \pm 0.4) \times 10^{20}$ cm^{-2}, slightly higher than the Galactic value reported from 21 cm measurements. On the other hand, the column density of neutral oxygen remained consistent regardless of which form is adopted for the soft X-ray continuum, i.e. for the TBNEW absorption model, then $N_O = (7.0 \pm 0.5) \times 10^{17}$ cm^{-2} (for the blackbody case) vs. $N_O = (6.5 \pm 0.3) \times 10^{17}$ cm^{-2} (for the COMPTT case). Thus when the soft X-ray spectrum is modeled with the Comptonized disk spectrum, due to the higher implied N_H values, the relative abundances are lower, largely consistent with the Solar values. Thus for Oxygen, the relative abundances with respect to the Solar values of Wilms et al. (2000) are $A_O = 1.20 \pm 0.04$ (for TBNEW) and $A_O = 1.10 \pm 0.08$ (for ISMABS) respectively.

4.2.1. The Form of the Soft X-ray Excess

Finally we note the continuum parameters associated with the COMPTT model. As the hard powerlaw constrained primarily above 2 keV is not well determined, its photon index has been fixed $\Gamma = 1.8$ (close to the best-fit value obtained for the EPIC-pn data, Nardini et al. 2016), with a corresponding photon flux

(normalization) at $1\,\mathrm{keV}$ of $N_\mathrm{PL} = (9.33 \pm 0.13) \times 10^{-3}\,\mathrm{photons\,cm^{-2}\,s^{-1}}$. For the Comptonized disk spectrum, an input temperature for the seed photons of $kT_\mathrm{in} = 20\,\mathrm{eV}$ is assumed, which may be reasonable for the emission from the inner optically thick disk around a black hole of mass $1.5 \times 10^8\,\mathrm{M_\odot}$ in Ark 120, with a bolometric luminosity of $2 \times 10^{45}\,\mathrm{erg\,s^{-1}}$, as determined from the broad-band SED (Porquet et al. 2016), which suggests accretion occurs at a rate of at least 10% of the Eddington value. These input seed disk photons are then assumed to be upscattered by a warm scattering medium, which we initially assume has an electron temperature of $kT_\mathrm{e} = 2\,\mathrm{keV}$; for this temperature the optical depth required to account for the soft excess is $\tau = 3.6 \pm 0.3$. However kT_e and τ are largely degenerate upon each other; if instead we adopt a lower temperature of $kT_\mathrm{e} = 0.5\,\mathrm{keV}$ for the Comptonizing electrons, then a higher optical depth of $\tau = 8.5 \pm 0.5$ is obtained. In either case, the soft excess corresponds to between $\sim 40 - 50\%$ of the total unabsorbed 0.4–2.0 keV band flux of $4.5 \times 10^{-11}\,\mathrm{erg\,cm^{-2}\,s^{-1}}$. Note that the COMPTT model produces a similar goodness of fit compared to the simple powerlaw plus blackbody model, given the relatively narrow band of the RGS spectrum.

A further more detailed discussion into the nature of the soft excess will be presented in a subsequent paper (Porquet et al. 2016), which will investigate the broadband XMM-Newton and *NuSTAR* observations, as well as the modeling of the optical to hard X-ray SED obtained from simultaneous data as part of the 2014 campaign.

5. The Emission Line Spectrum

Having adequately described the Galactic line of sight absorption towards Ark 120, the intrinsic emission spectrum of Ark 120 was then investigated. It is known that Ark 120 is a bare Seyfert 1, which contains no intrinsic absorption associated with the AGN, such as a warm absorber, which is also confirmed later in Section 5.5 from the contemporary 2014 observations. However one open question is whether the AGN is truly bare, or indeed whether there is evidence for emission from photoionized gas surrounding the AGN instead of absorption along our line of sight through the AGN, as might be expected in the context of AGN orientation dependent Unified Schemes (Antonucci 1993, Urry & Padovani 1995).

As a baseline model, the powerlaw plus blackbody continuum model was adopted, using the TBNEW model for the Galactic ISM absorption, with parameters reported in Table 2 and described in the previous section. Note that any dependency of the emission line spectrum on either the continuum form or the Galactic ISM model was checked and the subsequent parameters found to be consistent within errors. To provide an initial inspection of the contribution of any emission component, the summed 2014 RGS spectrum was first binned to a more coarse resolution of $\Delta\lambda = 0.1\,\mathrm{\AA}$ per spectral bin. This is a little worse than the intrinsic resolution of the RGS, which is typically $\Delta\lambda = 0.06 - 0.08\,\mathrm{\AA}$ (FWHM) over the 6–35$\,\mathrm{\AA}$ bandpass, but serves to highlight any prominent emission lines in the spectrum.

The RGS spectrum binned to this resolution is shown in Figure 5. The baseline continuum and Galactic absorption model overall provides a very good description of the shape of the RGS spectrum (see upper panel), however several strong positive deviations at $> 3\sigma$ level are apparent in the lower panel. Indeed the fit

statistic of the baseline model to the binned RGS spectrum is poor, with $\chi^2_\nu = 464.4/273 = 1.701$, formally rejected with a corresponding null hypothesis probability of 4.1×10^{-12}. Indeed the addition of seven Gaussian emission lines to the model significantly improves the fit statistic to $\chi^2_\nu = 296.3/254 = 1.165$, which is now statistically acceptable (null hypothesis probability of 3.5×10^{-2}). The centroids of the Gaussian profiles are close to several strong expected K-shell lines of N through to Mg; their centroid energies and likely identifications are:- 502 ± 2 eV (N VII Lyα), 568 ± 2 eV (O VII Heα), 654 ± 1 eV (O VIII Lyα), 865 ± 5 eV (Fe XVIII $3d \rightarrow 2p$ or O VIII RRC), 905 ± 4 eV (Ne IX Heα), 1343 ± 9 eV (Mg XI Heα) and 1476 ± 9 eV (Mg XII Lyα). Thus most of the emission lines appear to be associated with the He and H-like transitions of abundant elements. Several of the He-like lines appear to be resolved, especially for O VII, which when modeled with a single Gaussian requires a line width of $\sigma = 6.8 \pm 1.4$ eV. If these line widths are intrinsic, they would imply a significant degree of velocity broadening, with FWHM values in the range $\sim 5000 - 8500$ km s^{-1}. On the other hand, the widths may be the result of a blend of contributions from the forbidden, intercombination and resonance emission components associated with the triplet emission, which is investigated further in Section 5.3.

5.1. The High Resolution Line Spectrum

In order to provide a more accurate parameterization of the emission line spectrum and the line profiles, we reverted back to the spectrum binned at a finer resolution which adopted spectral bins of width $\Delta\lambda = 0.03$ Å over-sampling the FWHM resolution of the RGS by a factor of $\times 2 - 3$. The multiple spectral panels in Figure 6 show the data/model ratio of the RGS spectrum at this resolution to the baseline absorbed (TBNEW) continuum model, over the 0.4–1.6 keV range, whereby the expected rest energies or wavelengths of the main emission lines are marked with vertical dashed lines on the panels. The above emission line profiles are revealed in the residuals, in particular spectral structure is resolved around the He-like triplets especially from O VII and Ne IX. Furthermore positive residuals are also present in the region of the He-like N VI triplet around ~ 430 eV, although this part of the spectrum has been more coarsely binned by a factor of $\times 3$ as the signal to noise of the spectrum declines below 0.5 keV.

As before, the fit statistic improves considerably, now upon the addition of 8 Gaussian line profiles including the emission from N VI, with the fit statistic decreasing substantially from $\chi^2_\nu = 1344.0/936$ without any line emission (null hypothesis probability of 3.6×10^{-17}) to $\chi^2_\nu = 1087.3/914$ with the lines included. Initially the He-like line profiles have been modeled with single broad Gaussian emission lines and their properties, along with the H-like emission lines, are reported in Table 4. For instance the O VII profile is resolved with a width of $\sigma = 6.8^{+1.5}_{-1.2}$ eV, noting that the fit is significantly worse (by $\Delta\chi^2 = 68.1$) if the line width is restricted to $\sigma < 1$ eV. Similar widths are also derived from the other He-like profiles (although Mg XI is less well determined, as is its centroid energy). The centroid energy of the O VII line at $568.2^{+1.7}_{-1.6}$ eV suggests an identification with the intercombination emission from He-like Oxygen, which may imply a high electron density (Porquet & Dubau 2000, Porquet et al. 2010), which is discussed further later. The N VI triplet (seen in the upper panel of Figure 6) is similar in this regard, the line centroid energy of 428.4 ± 2.3 eV is consistent with the majority of the emission originating from the intercombination

transitions (near 426.3 eV), but is inconsistent with the expected energies of the forbidden (at 419.8 eV) and resonance (430.7 eV) emission lines. Conversely the centroid energy of the He-like triplet of Ne IX measured at 904.8 ± 3.6 eV is consistent with the expected energy of the forbidden line at 905.1 eV, but appears inconsistent with the positions of the intercombination and resonance lines at 914.8 eV and 922.0 eV respectively. The modeling of the He-like triplets and the question of whether they are intrinsically velocity broadened or instead arise from a combination of the forbidden, intercombination and resonance components is discussed later in Section 5.3.

The H-like lines from N VII, O VIII and Mg XII are all significantly detected close to their expected rest frame energies or wavelengths, with only the H-like line of Ne X not being formally detected, as listed in Table 4. At first sight, unlike the emission from the He-like ions, the H-like lines generally appear to be unresolved, with the corresponding upper-limits given to their 1σ Gaussian widths in Table 4. The H-like profiles are also discussed in further detail in the next section. The only uncertain identification is for the emission measured at 864.7 ± 1.9 eV, which may be associated to L-shell emission from iron (e.g. Fe XVIII $3p \rightarrow 2s$), but could also contain a contribution from the radiative recombination continuum (RRC) of O VIII.

None of the higher order lines are detected, generally with tight upper limits. For instance the upper-limit on the flux from the O VII Heβ emission ($E = 661 - 666$ eV) is $< 0.92 \times 10^{-5}$ photons cm^{-2} s^{-1} (or an equivalent width of < 0.2 eV), which implies a ratio of the Heα/Heβ emission of > 20. Likewise the ratio of fluxes of O VIII Lyα to Lyβ lines is > 5. This may imply the line emission is associated with recombination (and subsequent radiative cascade) following photoionization rather than radiative decay following photo-excitation, as the latter process generally boosts the strengths of the higher order (e.g. Lyβ and Heβ) emission lines (see Kinkhabwala et al. 2002). If this is the case, detectable RRC emission may be expected. The data are consistent with the presence of the O VIII RRC as noted above, with a total flux of 1.4×10^{-5} photons cm^{-2} s^{-1}, while the limit obtained on the temperature is $kT < 10$ eV (or $< 6 \times 10^4$ K). Formally the O VII RRC is not detected, with an upper limit of $< 2.3 \times 10^{-5}$ photons cm^{-2} s^{-1} on the photon flux. Note that in the latter case, it may be difficult to detect an RRC feature, due to the large velocity width of the O VII emission, resulting in a weak and broadened profile. Overall, the line emission is consistent with a photoionized plasma, a view supported by the XSTAR emission modeling presented later in Section 6.4.

The X-ray spectrum does not allow for any strong contribution from a collisionally ionized plasma, which appears consistent with the lack of any strong iron L-shell emission lines. Furthermore, any resonance components in the He-like triplets are weak (Section 5.3), which generally implies a low temperature plasma. For a $kT = 0.5$ keV temperature plasma with Solar abundances, the upper limit on the luminosity of any emission from a collisionally ionized plasma is $< 2.5 \times 10^{41}$ erg s^{-1}, which is $< 0.25\%$ of the total 0.4–2.0 keV band soft X-ray luminosity from the AGN. In comparison the total luminosity derived from the Gaussian emission line profiles is $\sim 1.0 \times 10^{42}$ erg s^{-1}, thus any thermal plasma contributes less than 25% of the total line emission. In practice, the contribution of a collisionally ionized plasma towards the observed emission lines is likely much smaller, as a significant proportion of the luminosity of any collisional plasma arises in the thermal bremsstrahlung continuum, rather than in the lines themselves.

5.2. Emission Line Profiles

In order to derive further constraints on the kinematics of the line emitting gas, velocity profiles of six of the strongest emission lines were constructed, from adopting the data/continuum model ratios for each line and transposing them into velocity space, with respect to their expected lab rest frame energies, with negative values denoting blueshift. For the He-like lines, velocity profiles were constructed for N VI, O VII and Ne IX, which are the best defined He-like complexes (Mg XI being poorly constrained in the RGS). For the N VI and O VII He-like line complexes, the velocities were centered (at zero velocity) on the expected positions of the intercombination emission, as from the previous fits it appeared that both of these line profile centroids lie close to these transitions. In contrast, the Ne IX profile is centered (with zero velocity) at the expected position of the forbidden line at 905.1 eV, as also indicated in the above spectral fits.

Velocity profiles were also created for the H-like (Lyman-α) emission lines of N VII, O VIII and Mg XII, centered at zero velocity on the expected centroid energy of the emission line doublets (the separation of which is unresolved in the RGS data). The velocity profiles of the three H-like and three He-like profiles are plotted in Figure 7. The profiles have initially been fitted with single Gaussians, with the centroid position and 1σ width (in velocity space) as well as the Gaussian normalization (flux) allowed to vary. For the He-like complexes, the vertical (dashed-dotted) lines indicate the relative positions in velocity space of the resonance, intercombination and forbidden emission line components compared to the line centroids, while for the H-like profiles, the expected center position of the doublet is marked with a vertical line (at zero velocity). The results of these single Gaussian fits to the six line profiles are also tabulated in Table 5.

The centroid emission of the H-like profiles are generally close to zero velocity and do not appear to be resolved in terms of their widths compared to the resolution of the RGS spectrometer. Indeed, after correcting for the instrumental width due to the response function of the RGS, only upper-limits are obtained for the intrinsic velocity widths of the H-like N VII, O VIII and Mg XII lines. For instance the limit on the width of the N VII profile is $\sigma < 290\,\mathrm{km\,s^{-1}}$ (or FWHM, $< 680\,\mathrm{km\,s^{-1}}$), while for O VIII the velocity width is restricted to $\sigma < 470\,\mathrm{km\,s^{-1}}$ (or FWHM, $< 1100\,\mathrm{km\,s^{-1}}$); see Table 5 for details. There is an marginal indication that the line centroids are slightly blueshifted in the case of N VII and O VIII (with velocities of $v_{\mathrm{out}} = -410 \pm 120\,\mathrm{km\,s^{-1}}$ and $-250 \pm 130\,\mathrm{km\,s^{-1}}$ respectively). There is also a hint of positive residuals on the blue-wing of the N VII line (between -2000 to $-3000\,\mathrm{km\,s^{-1}}$) and on the red-wing (near $+2000\,\mathrm{km\,s^{-1}}$) of the O VIII profile, although neither are statistically significant. Thus although we cannot exclude an underlying broad component to either of these profiles, it is likely to be weak. Finally for the O VIII profile, there appears to be a marginally significant (at the $\sim 3\sigma$ level) absorption feature, observed at $E = 0.643\,\mathrm{keV}$ and redshifted by $+4500\,\mathrm{km\,s^{-1}}$ with respect to the O VIII Ly-α centroid. However this may be spurious, as no other absorption lines are associated to any of the other profiles at a similar velocity.

5.3. The He-like triplets

In contrast, the He-like profiles shown in Figure 7 all appear significantly broadened when fitted with a single Gaussian profile, with intrinsic 1σ velocity widths of between $\sigma = 3200 - 4000\,\mathrm{km\,s^{-1}}$ typically

(see Table 5 for the corresponding FWHM values). In comparison the contribution of the width from the instrumental resolution of the RGS is negligible at the positions of these lines. The centroid of the Gaussian profile of the N VI emission is close to that of the intercombination transitions, albeit with a small blueshift of $v_{\mathrm{out}} = -1500 \pm 1000\,\mathrm{km\,s^{-1}}$. Likewise the O VII profile is centered at the position of the intercombination emission, with no velocity shift required, which is limited to $< 730\,\mathrm{km\,s^{-1}}$. Note that for the broad O VII profile to be primarily associated to the forbidden line would instead require a significant blueshift of $-4000\,\mathrm{km\,s^{-1}}$. However there may still be some contribution of the forbidden line to the overall O VII profile, as some excess is observed near its expected position in the profile. In contrast the broad Ne IX Gaussian appears centered at the forbidden line, with any velocity shift of the profile limited to $< 710\,\mathrm{km\,s^{-1}}$.

Next, the He-like profiles were modeled using a combination of the forbidden, intercombination and resonance components, with the widths of these components limited to the instrumental RGS resolution, i.e. they are initially assumed to be intrinsically narrow and the overall He-like complex consists of a blend of these narrow lines. The fit with narrow lines to the profiles are displayed in the left hand panels of Figure 8. In the case of N VI, which is the least well determined of the three He-like line profiles, an acceptable fit to the profile of $\chi^2/\mathrm{dof} = 27.0/25$ is obtained from the combination of three narrow components. This is comparable to the fit obtained above with a single broad profile, where $\chi^2/\mathrm{dof} = 26.5/28$. However in order to model the profile with 3 narrow components, a significant blueshift (of the order $-2000\,\mathrm{km\,s^{-1}}$) is required, as can be seen in panel (a) in Figure 8 with respect to their expected positions. Nonetheless, allowing the intercombination emission to have some intrinsic width does improve the fit statistic somewhat to $\chi^2/\mathrm{dof} = 20.7/25$, with an intrinsic width of $\sigma_{\mathrm{v}} = 1840 \pm 820\,\mathrm{km\,s^{-1}}$ (see Fig 8, panel b).

In contrast the O VII profile is poorly modeled ($\chi^2/\mathrm{dof} = 92.1/52$) with a combination of 3 narrow lines, as is seen in Figure 8(c), where significant flux is left unmodeled by the narrow emission lines. Thus allowing a broad component (while retaining a possible contribution from any narrow emission if required), results in a significant improvement in the fit statistic to $\chi^2/\mathrm{dof} = 37.7/51$. The line width then becomes significantly broadened as before, with the line centroid consistent with the expected position of the intercombination emission. A weak contribution from a narrow forbidden line may still be present in the model, as can be seen near $+4000\,\mathrm{km\,s^{-1}}$ (wrt the intercombination emission) in Figure 8(d), which shows the composite narrow plus broad profile. Likewise, the Ne IX line profile is also poorly modeled with a combination of three narrow line components, with $\chi^2/\mathrm{dof} = 73.5/34$ and significant line flux is left on both the red and the blue side of the narrow forbidden line (Figure 8, panel e). Thus allowing the width of the forbidden line to increase results in a substantial improvement in the fit statistic to $\chi^2/\mathrm{dof} = 30.9/33$, while the contribution of any narrow intercombination and resonance lines are negligible (Figure 8f).

It is also possible that the line triplets are composed of a blend of broadened emission from each of the components, i.e. with the same velocity width as might be expected if they originate from within the same zone of gas. To test this and to determine the relative contribution of the three components towards the overall broad profiles, each He-like profile was fitted with three Gaussian components near the expected positions of the forbidden, intercombination and resonance emission lines. A common (tied) velocity width was adopted between each of the Gaussians. Although the subsequent three Gaussian fits were statistically identical to a fit with a single broad Gaussian profile as above, the results give an indication of the relative

contribution of each component towards the overall profile. The results of this deconvolution are shown for each triplet in Table 5. For the O VII triplet, the emission can be equally composed of contributions from the forbidden, intercombination and resonance emission. The line width is then somewhat lower than for a single broad Gaussian, but is still significantly broadened, with $\sigma_{\rm v} = 2000^{+1200}_{-800}\,{\rm km\,s^{-1}}$. In contrast the Ne IX broad profile is dominated by the forbidden emission, which is not surprising as the overall line profile is centered very near the expected position of the forbidden line. The resulting common line width in this case is $\sigma_{\rm v} = 2300^{+1800}_{-1100}\,{\rm km\,s^{-1}}$ (Table 5).

Thus for the He-like lines, the broad component appears to dominate these profiles, with any narrow line contribution representing a relatively small component of the total line flux. The high flux ratio of the intercombination to forbidden emission, for at least the N VI and O VII triplets, suggests that the electron density of the gas may be relatively high. In contrast, the velocity widths of the highest ionization H-like lines are generally narrow or unresolved, while some profiles may have a modest outflow velocity.

5.4.   Constraints on the Line Emission in the Chandra HETG Spectrum

In addition to the deep RGS exposure, a 120 ks exposure was also obtained with Chandra/HETG over the same time frame. Given the much shorter HETG exposure and lower area at the lowest energies, the signal to noise below 1 keV does not provide any additional constraints on the O VII or Ne IX line emission. Although the primary purpose of the *Chandra* exposure was to measure the Fe K profile at high resolution, the HETG does provide additional constraints on any possible emission from Mg, Si and S above 1 keV, where in particular its higher resolution compared to the RGS makes the HETG more sensitive to any narrow components of the line emission.

The most significant soft X-ray line emission detected in the HETG spectrum arises from the Mg XI He-like triplet, which is shown in Figure 9. Indeed at this energy, the resolution of the HEG spectrum is a factor $\times 8$ higher compared to the RGS. Significant line emission (at $> 99.9\%$ confidence with $\Delta C = 14.8$) is revealed in the HEG spectrum just bluewards of the expected position of the Mg XI forbidden line (at $E_{\rm lab} = 1331.1\,{\rm eV}$), with a measured rest energy of $E = 1333.5^{+1.3}_{-1.5}\,{\rm eV}$ (see Table 4). The equivalent width of the line is $2.2 \pm 1.0\,{\rm eV}$, which is consistent with the tentative detection of the Mg XI line in the RGS spectrum at lower resolution. Interesting the forbidden line profile appears somewhat broadened in the *Chandra* spectrum, compared to the HEG FWHM resolution of $320\,{\rm km\,s^{-1}}$ at this energy. Indeed the best fit line width is $\sigma = 2.0^{+1.3}_{-0.8}\,{\rm eV}$, corresponding to a velocity width of $\sigma_{\rm v} = 450^{+290}_{-180}\,{\rm km\,s^{-1}}$ (or $1050^{+680}_{-420}\,{\rm km\,s^{-1}}$ at FWHM); see Tables 4 and 5. This is consistent with the widths of the narrow H-like components measured above in the RGS, which are largely unresolved at lower resolution; e.g. O VIII Lyman-α has a velocity width constrained to $\sigma_{\rm v} < 470\,{\rm km\,s^{-1}}$ in the RGS spectrum.

Thus the forbidden emission detected and resolved in the *Chandra* spectrum appears consistent in origin with the narrow line emitting gas revealed in the RGS spectrum. Curiously the Mg XI line profile appears slightly blue-shifted with respect to the expected position of the forbidden line, with an overall blue-shift of $v_{\rm out} = -540^{+340}_{-290}\,{\rm km\,s^{-1}}$. This is also consistent with the narrow line profiles observed in the

RGS, which may also have a modest blueshift; e.g. N VII Ly-α with $-410 \pm 120 \, \mathrm{km \, s^{-1}}$ or O VII Ly-α with $-250 \pm 130 \, \mathrm{km \, s^{-1}}$ (see Table 5 and Figure 7). Thus the narrow line gas may be associated to a slight outflow velocity, while the small line widths suggest that it is located further from the nucleus than for the broad line profiles. Note that unlike the detection of the forbidden emission, there is no detection of emission from either the intercombination or resonance components of the Mg XI line triplet (see Figure 9), with upper limits of $< 0.4 \, \mathrm{eV}$ and $< 1.5 \, \mathrm{eV}$ on the equivalent widths respectively. This suggests that the narrow lined emission originates primarily from lower density gas (given the dominance of the forbidden over the intercombination emission); the line diagnostics from the triplets will be discussed further in Section 6.

Aside from at Mg XI (and also at the iron Kα line, which will be presented by Nardini et al. 2016), there are no other significant detections of line emission in the HETG spectrum. There are some weak indications of emission associated with the forbidden lines of Si XIII and S XV, although neither of these are formally significant (with $\Delta C = 2$ and $\Delta C = 5$), with upper limits of $< 1.1 \, \mathrm{eV}$ and $< 2.5 \, \mathrm{eV}$ respectively on their equivalent widths. Neither are any of the H-like lines from Mg, Si or S detected. Generally this is expected given the continuum dominated nature of Ark 120, while it is the exceptionally deep RGS exposure that has enabled the detection of the soft X-ray line emission for the first time from this AGN.

5.5. Is there any Warm Absorption towards Ark 120?

In addition to the emission, here we place limits on any intrinsic ionized absorption towards Ark 120. We included a Solar abundance XSTAR multiplicative table of photoionized absorption spectra in the spectral model fitted to the RGS at the rest frame of the AGN, while the outflow velocity was allowed to vary between $\pm 3000 \, \mathrm{km \, s^{-1}}$ to allow for any velocity shift. A turbulence velocity of $\sigma = 300 \, \mathrm{km \, s^{-1}}$ was chosen, to account for any narrow absorption lines. The ionization parameter of the absorption table was varied between $\log \xi = 0 - 3$[3] to allow for the typical range in ionization seen towards other Seyfert 1s, with prominent warm absorption components (Kaspi et al. 2002, Blustin et al. 2005, Detmers et al. 2011, Reeves et al. 2013, Di Gesu et al. 2015). The total N_{H} column was recorded for each value of the ionization parameter, in increments of 0.1 in $\log \xi$ space. Tight limits were placed on the total absorbing column density, of between $N_{\mathrm{H}} < 1.8 \times 10^{19} \, \mathrm{cm^{-2}}$ and $N_{\mathrm{H}} < 3.4 \times 10^{19} \, \mathrm{cm^{-2}}$ over the ionization range of $\log(\xi / \mathrm{erg \, cm \, s^{-1}}) = 0 - 2$, with a less stringent constraint towards higher ionization values ($N_{\mathrm{H}} < 6.0 \times 10^{20} \, \mathrm{cm^{-2}}$ for $\log(\xi / \mathrm{erg \, cm \, s^{-1}}) = 3$). Furthermore the limits on the total O column, over the ionization range $\log(\xi / \mathrm{erg \, cm \, s^{-1}}) = 0 - 2$ (where typically most of the absorption due to O VII and O VIII is expected to occur), varies between $N_{\mathrm{O}} < 1.2 \times 10^{16} \, \mathrm{cm^{-2}}$ and $N_{\mathrm{O}} < 3.4 \times 10^{16} \, \mathrm{cm^{-2}}$.

Indeed upon inspection of the RGS spectra (Figure 6) there are no apparent absorption features at positions close to the expected resonance transitions of the strongest lines in the soft X-ray band. The findings and constraints on the column density of the absorption here are consistent with those of Vaughan et al.

---

[3] The ionization parameter is defined here as $\xi = L_{\mathrm{ion}} / nr^2$, where L_{ion} is the ionizing luminosity measured between 1–1000 Rydberg, n is the electron density and r is the radial distance from the X-ray source. The units of the ionization parameter are $\mathrm{erg \, cm \, s^{-1}}$.

(2004), who published their findings from a single orbit (112 ks RGS exposure) XMM-Newton observation taken in 2003 and whom also found no evidence for any intrinsic X-ray absorption towards Ark 120. Furthermore there is no known UV absorber associated with Ark 120 (e.g. Crenshaw et al. 1999, Crenshaw & Kraemer 2001). This confirms Ark 120 as the prototype bare Seyfert 1 AGN, with no known intrinsic absorption along the line of sight towards the AGN.

6. Discussion

6.1. The Origins of the Ionized Soft X-ray Emission in Ark 120

While there is no intrinsic X-ray absorption towards Ark 120 (aside from the neutral ISM absorption due to the Milkyway), the high signal to noise RGS spectrum has revealed several broad and narrow emission line profiles associated to the AGN. As shown in Section 5, these broad profiles are associated with the He-like emission from N VI, O VII and Ne IX with velocity widths in the range from 4000–8000 km s^{-1} (FWHM). In addition, the line profile modeling in Section 5.3 appears to exclude the possibility of the He-like triplets being composed of purely a blend of narrow unresolved emission lines from the forbidden, intercombination and resonance components, with the intrinsic velocity widths being resolved by the RGS (see Figure 8). In contrast the H-like profiles from N VII, O VIII and Mg XII are narrow, for instance for the O VIII Lyα emission the upper limit on the Gaussian velocity width is $\sigma < 470$ km s^{-1}.

Thus while there is no direct absorption along the line of sight associated to the AGN (see also Vaughan et al. 2004, Matt et al. 2014), the fact that there is significant soft X-ray line emission associated with Ark 120 suggests the AGN is not intrinsically bare. Thus the lack of absorption may just indicate that we are viewing the AGN along a preferential line of sight, with relatively little ionized gas along our direct view. The detection of narrow soft X-ray emission from many Seyfert galaxies, associated with photoionized or photoexcited gas, has proven common from grating observations of obscured AGN (Kinkhabwala et al. 2002), with the origin likely to be on scales consistent with the AGN Narrow Line Region (NLR) and perhaps arising from a large scale outflow. However recent observations are now also revealing the detections of broad soft X-ray line profiles from several Seyfert 1 galaxies, with velocity widths of several thousand km/s, suggesting an origin commensurate with the AGN Broad Line Region (BLR). Examples include NGC 4051 (Ogle et al. 2004, Pounds & Vaughan 2011), Mrk 335 (Longinotti et al. 2008), Mrk 841 (Longinotti et al. 2010), 3C 445 (Reeves et al. 2010), Mrk 509 (Detmers et al. 2011), MR 2251-178 (Reeves et al. 2013) and NGC 5548 (Kaastra et al. 2014).

Indeed another AGN that bares some similarity to Ark 120 is the bare Seyfert 1 galaxy, Mrk 590. Here *XMM-Newton* and *Chandra* showed no intrinsic absorption, but the presence of narrow ionized emission associated with highly ionized iron (Fe XXV and Fe XXVI) as well as from ionized Oxygen (O VIII); see Longinotti et al. (2007). In addition, the extended soft X-ray emission detected in the *Chandra* image of Mrk 590 implies the presence of ionized gas on larger (kpc) scales. The overall picture may be similar to what is observed in Ark 120, namely that little ionized gas is detected along the line of sight, but evidence for photoionized gas is still seen from the circumnuclear gas out of the direct view. In Ark 120, the detection

of both narrow and broad lines implies the existence of soft X-ray emitting gas over a wide range of spatial scales, from the sub-pc BLR gas out to the more distant NLR, with the narrow highly ionized H-like emission possibly associated to the warm scattering gas on larger scales. In the following section, we attempt to quantify the location and physical properties of the soft X-ray emitting gas in Ark 120.

6.2. Constraints from the He-like line triplets

The lack of intrinsic X-ray absorption towards Ark 120 allowed a clean measurement of the emission from the He-like triplets. Given the constraints on the He-like line triplets, we can place an estimate on the density and subsequently infer the likely radial location of the emitting gas. The line ratios $G = (x + y + z)/w$ and $R = z/(x + y)$ give a measure of the temperature and density of the gas, where z corresponds to the forbidden line, $(x + y)$ to the intercombination emission and w to the resonance line (Porquet & Dubau 2000). Taking the ratios of the fluxes of the line components measured from the O VII triplet (Table 5), then $R = 1.1 \pm 0.6$, resulting from a relatively equal contribution of the broad forbidden and intercombination components. This indicates that the gas is of relatively high density. From the calculations of Porquet & Dubau (2000), this ratio corresponds to an electron density of $n_{\mathrm{e}} \sim 10^{11} \, \mathrm{cm}^{-3}$. On the other hand the high G ratio, of $G = 2.1 \pm 1.0$, indicates that the gas being photoionized rather than collisionally ionized, with a temperature of $T < 10^6$ K. Note that photoionization rather than photo-excitation appears the more dominant mechanism in Ark 120, given the relative weakness of the higher order emission lines (see Fig 5, Kinkhabwala et al. 2002); for instance for O VII the ratio of the Heα to Heβ emission is > 10.

In contrast for the He-like triplet of Ne IX, the forbidden line appears to dominate over any intercombination emission (see Table 5), as generally the Ne IX triplet is more sensitive towards higher densities compared to O VII. Thus the R ratio of $R > 3.3$ implies a limiting density of $n_{\mathrm{e}} \lesssim 2 \times 10^{11} \, \mathrm{cm}^{-3}$. So for Ark 120, the broad lined soft X-ray emitting gas appears consistent with a density in the range from $10^{11} \lesssim n_{\mathrm{e}} \gtrsim 2 \times 10^{11} \, \mathrm{cm}^{-3}$. The G ratio from the Ne IX triplet is $G > 3.8$, consistent with a photoionized plasma. Note that the constraints on R obtained from the N VI triplet are consistent with this, with a resulting lower limit on the density of $n_{\mathrm{e}} > 10^{10} \, \mathrm{cm}^{-3}$.

6.3. The Ionization State and Location of the Gas

Thus the above density would seem to imply an origin of the broad line emission consistent with the optical BLR (Davidson & Netzer 1979). The ionization of the emitter can also be constrained, given the measured line flux ratio of O VII Heα / O VIII Ly$\alpha \sim 10$, e.g. Table 4. Indeed from fitting an XSTAR emission model with a density of $n_{\mathrm{e}} = 10^{11} \, \mathrm{cm}^{-3}$ to model the O VII emission (see Section 6.4), an ionization parameter of $\log(\xi/\mathrm{erg \, cm \, s}^{-1}) = 0.5$ is required in order for the less ionized He-like emission to dominate over the H-like emission.

From this an estimate of the radial distance of the emitter can be obtained via the definition of the ionization parameter, i.e. $r = (L_{\mathrm{ion}}/\xi n_{\mathrm{e}})^{1/2}$, where L_{ion} is the $1 - 1000$ Rydberg luminosity and n_{e} is

the electron density. From the broad-band UV to hard X-ray SED, the ionizing luminosity of Ark 120 is $L_{\rm ion} \sim 10^{45}\,{\rm erg\,s^{-1}}$ (Porquet et al. 2016). If we adopt a density of $n_{\rm e} = 10^{11}\,{\rm cm^{-3}}$ from the above considerations, then the emitting radius is $r = 5 \times 10^{16}\,{\rm cm}$ (or $\sim 0.01\,{\rm pc}$), again consistent with typical BLR radii (Kaspi et al. 2005). Furthermore the distance to the optical BLR, inferred from time delays of the Hβ line wrt to the continuum in Ark 120 is $\tau \sim 40$ light days (Peterson & Gaskell 1991, Wandel, Peterson & Malkan 1999), equivalent to a distance of $10^{17}\,{\rm cm}$. The radius of the emission can also be estimated from the O VII or Ne IX velocity widths of $\sigma \sim 2000\,{\rm km\,s^{-1}}$ or a FWHM of $\sim 5000\,{\rm km\,s^{-1}}$, adopting the more conservative lower value from the triplet deconstruction (see Table 5). Assuming a standard virial relation between the black hole mass and the radius r, of $3\sigma^2 = GM/r$ and adopting a black hole mass of $1.5 \pm 0.2 \times 10^8\,{\rm M_\odot}$ for Ark 120 from reverberation mapping (Peterson et al. 2004), gives a radius of $r \sim 10^{17}\,{\rm cm}$, consistent with the above estimates.

In comparison the optical Hβ FWHM line width of Ark 120 is $5850 \pm 480\,{\rm km\,s^{-1}}$ (Wandel, Peterson & Malkan 1999), which is similar to (or slightly smaller) than the typical X-ray broad line widths measured here. Furthermore the core of the 6.4 keV iron Kα emission line is also resolved in the simultaneous Chandra/HETG spectrum, with a FWHM width of $4500^{+2500}_{-1500}\,{\rm km\,s^{-1}}$ (Nardini et al. 2016), consistent with the above estimates. Thus the observations suggest that the soft X-ray broad emission lines originating from a higher ionization phase of the AGN BLR, with radii in the typical range from $5 \times 10^{16} - 10^{17}\,{\rm cm}$.

In contrast the H-like profiles measured in the spectra from N, O and Mg appear narrow and are unresolved by the RGS – see Figure 7 and Table 5. The constraints on the density of the narrow lined emitting gas are not as tight as for the broad lines, with the Mg XI triplet measured from *Chandra* (forbidden dominating over intercombination with $R > 3.2$) indicating $n_{\rm e} < 10^{12}\,{\rm cm^{-3}}$. Thus although we cannot directly measure the density of the narrow line emitting gas from line diagnostics, we can calculate its likely radial location from the limits on the velocity widths. If we take the line width for the resolved Mg XI forbidden line from the *Chandra* spectrum, with $\sigma = 450^{+290}_{-180}\,{\rm km\,s^{-1}}$, then the likely radius of the emitting gas is on pc scales. Note this is also consistent with the limits on the widths of the narrow lines seen in the RGS, e.g. for the O VIII Lyα line then $\sigma < 470\,{\rm km\,s^{-1}}$. For comparison, the expected distances of the torus and of the Narrow Line Region (NLR) are about 3 pc and 100 pc, using the following formula of Krolik & Kriss (2001) and Mor, Netzer & Elitzur (2009) respectively:

$$R_{\rm torus} \sim L_{\rm ion,44}^{1/2} \qquad (pc) \tag{1}$$

$$R_{\rm NLR} = 295 \times L_{46}^{0.47\pm0.13} \quad (pc). \tag{2}$$

Thus, unlike for the broad line emitting gas, the narrow line X-ray emission appears consistent with radial locations commensurate with the pc scale torus or innermost NLR. This is also at a similar location to some of the soft X-ray warm absorbers inferred in Seyfert 1 AGN (see Tombesi et al. 2013 and references therein), which may imply that we are viewing similar ionized gas in Ark 120 out of our direct line of sight.

6.4. The Covering Fraction and Geometry of the Gas

The luminosity of the soft X-ray line emission can also be used to calculate the global covering factor of the gas (see also Nucita et al. 2010). From the photoionization modeling, the normalization (or flux), κ_{xstar}, of an emission component is defined by XSTAR (Kallman et al. 2004) in terms of:

$$\kappa_{\mathrm{xstar}} = f \frac{L_{38}}{D_{\mathrm{kpc}}^2} \tag{3}$$

where L_{38} is the ionizing luminosity in units of 10^{38} erg s^{-1}, D_{kpc} is the distance to the AGN in kpc. Here f is the covering fraction of the gas with respect to the total solid angle, where $f = \Omega/4\pi$. For a spherical shell of gas, $f = 1$, while L is the quasar ionizing luminosity that illuminates the photoionized shell. The ionizing luminosity obtained from the best fit spectral model and corrected for the intervening Galactic absorption, is $L = 4.5 \times 10^{44}$ erg s^{-1} over the 1–1000 Rydberg band[4]. Thus for Ark 120 with $D = 133$ Mpc and for a spherical shell, the expected XSTAR normalization from above is $\kappa_{\mathrm{xstar}} = 2.5 \times 10^{-4}$. Hence for a given column density of gas, this sets the total luminosity of the soft X-ray photoionized emission.

As a first step, model emission line spectra were then generated with this overall normalization factor within XSTAR, which gives the predicted emission originating from a fully covering spherical shell of gas (with $f = 1$), illuminated by an AGN ionizing luminosity of L. The ionization of the gas was fixed at $\log(\xi/\mathrm{erg\,cm\,s}^{-1}) = 0.5$, consistent with the XSTAR fits to the lines (see below). Taking as an example the case of the strong O VII Heα broad emission line observed in the RGS spectrum, we then compared the observed line luminosity to that predicted by the XSTAR model and then used the ratio of the observed to predicted line luminosity to calculate the global covering fraction of the gas. From the Ark 120 spectrum, the observed luminosity of the broad O VII emission is $L_{\mathrm{OVII}} = 4.0 \pm 1.2 \times 10^{41}$ erg s^{-1}. In comparison, for a column density of $N_{\mathrm{H}} = 10^{21}$ cm^{-2}, the O VII luminosity predicted by the XSTAR model for a fully covering shell of gas is 1.2×10^{42} erg s^{-1}. The ratio of the observed to predicted luminosity then gives the geometric covering fraction of the emitter, which for $N_{\mathrm{H}} = 10^{21}$ cm^{-2} is $f = 0.33 \pm 0.10$. Similarly, for a higher column of $N_{\mathrm{H}} = 10^{22}$ cm^{-2}, the predicted O VII luminosity of a spherical shell is higher, with 3.6×10^{42} erg s^{-1} and thus the covering fraction is then lower, with $f = 0.11 \pm 0.03$.

To provide a more quantitative estimate of the covering fraction, the RGS spectrum was then fitted with the XSTAR emission models. In order to reproduce the strongest emission lines present in the Ark 120 spectrum, three different photoionized emission zones were required and their properties are summarized in Table 6. Two of these emission zones appear to be broadened (with $\sigma = 3000$ km s^{-1}); these are required to model (i) the broad O VII emission (as well as at N VI) and (ii) the broad Ne IX emission, with the lower ionization zone (with $\log \xi = 0.5 \pm 0.1$) responsible for O VII. A third, highest ionization zone ($\log \xi = 2.3 \pm 0.4$) with a narrow velocity width ($\sigma = 300$ km s^{-1}) is responsible for the narrow H-like lines, such as from O VIII Ly-α. The column density of the gas in emission is not known a priori (due to the lack of absorbing gas) and is highly degenerate with the emission normalization. Thus instead of directly

---

[4]Note that the ionizing luminosity returned from a broad-band fit to Ark 120 with the *XMM-Newton* EPIC and OM data, obtained from the OPTXAGN disk + corona model (Porquet et al. 2016, in preparation), is $\sim 10^{45}$ erg s^{-1}.

fitting both the column and the normalization of the XSTAR emission zones, the column density was varied over the range $3 \times 10^{20} < N_{\mathrm{H}} < 10^{22} \, \mathrm{cm}^{-2}$, adopting 8 different values and at each fixed N_{H} value the spectrum was refitted to obtain the normalization of the XSTAR component. Thus by comparing the observed normalization (κ_{obs}) of a fitted emission component with the predicted value from equation 3 (κ_{xstar}), the covering fraction for a given column can be calculated by $f = \kappa_{\mathrm{obs}}/\kappa_{\mathrm{xstar}}$.

The resulting plot of covering fraction vs. column for the O VII emission zone is shown in Figure 10, noting that similar results are also found for the Ne IX zone and the (narrow) O VIII zone (see Table 6). The overall trend is for the covering fraction of the gas to decrease with increasing column. This would be expected as increasing the column density of the gas clouds increases their soft X-ray luminosity, requiring the overall covering fraction to decrease in order to compensate. A minimum column density of $N_{\mathrm{H}} > 3 \times 10^{20} \, \mathrm{cm}^{-2}$ is required to reproduce the required O VII luminosity, if the gas is fully covering the AGN with $f = 1$. This fully covering scenario appears less likely, as the upper-limit to the line of sight column of soft X-ray warm absorbing gas towards Ark 120 is at least factor of $\times 10$ lower; with $N_{\mathrm{H}} < 3 \times 10^{19} \, \mathrm{cm}^{-2}$ for $\log(\xi/\mathrm{erg\,cm\,s}^{-1}) = 1$, see Section 5.5. Instead the covering fraction is likely to be lower, with no significant distribution of gas along the line of sight, allowing the column density out of the direct line of sight to be higher. Indeed once the column density approaches $N_{\mathrm{H}} = 10^{22} \, \mathrm{cm}^{-2}$, then the covering reaches a limiting value of $f = 0.1$. This corresponds to a likely *minimum* covering fraction of gas as increasing the column density above $N_{\mathrm{H}} > 10^{22} \, \mathrm{cm}^{-2}$ has little effect on the total line luminosity; i.e at these columns and higher, the emitting clouds become optically thick at soft X-rays, with little change in the resulting soft X-ray line luminosity.

6.5. X-ray Broad and Narrow Line Regions

Thus the above calculations, in order to reproduce the broad soft X-ray line emission, requires the emitting gas to have a typical column of up to $N_{\mathrm{H}} \sim 10^{22} \, \mathrm{cm}^{-2}$, with a covering fraction of at least 10% of 4π steradian and for the gas to lie out of the direct line of sight. The mass of the emitting gas implied from these calculations is $\sim 0.1 \, \mathrm{M}_{\odot}$, for $N_{\mathrm{H}} = 10^{22} \, \mathrm{cm}^{-2}$ and $f = 0.1$. Overall this scenario is similar to what is usually inferred from studies of the optical–UV BLR (Baldwin et al. 1995, Gaskell 2009), with the distribution of emitting BLR clouds likely non-spherical and following a flattened or disk-like geometry (Krolik et al. 1991, Eracleous & Halpern 2003). The latter distribution of emitting clouds can also account for the lack of absorption towards Ark 120 if the gas lies out of the direct line of sight and our view of the AGN is relatively pole-on compared to the plane of the disk. This may also be consistent with the morphology of the host spiral galaxy being relatively pole-on in Ark 120 (Nordgren et al. 1995). The opposite may be the case in AGN where variable X-ray obscuration events occur, when the line of sight can be intercepted by compact clouds consistent with observed BLR distances. Such X-ray obscuration events have been observed several Seyfert galaxies, such as in Mrk 335 (Longinotti et al. 2013), NGC 3227 (Lamer et al. 2003), NGC 1365 (Risaliti et al. 2005b, Braito et al. 2014), NGC 4051 (Terashima et al. 2009, Lobban et al. 2011), NGC 3516 (Turner et al. 2008) and NGC 5548 (Kaastra et al. 2014).

In contrast to the broadened emission, the kinematics of the narrow soft X-ray emission lines are consistent with arising from pc scale distances or higher. The typical column density and covering fraction of the narrow emission line gas is similar to broad lined gas; for a column of $N_{\mathrm{H}} = 1 \times 10^{21}\,\mathrm{cm}^{-2}$, the covering fraction is consistent with $f = 1$, while the covering fraction decreases to $\sim 10\%$ for $N_{\mathrm{H}} = 1 \times 10^{22}\,\mathrm{cm}^{-2}$. Thus the derived columns and covering fractions are thus likely too low to be commensurate with emission from a Compton thick pc-scale torus. However the origin of the gas in emission may arise from the AGN Narrow Lined Region (NLR) and is in general agreement with the typical columns and spatial locations of matter inferred along the line of sight in the warm absorbers that are observed in many other Seyfert 1 AGN (e.g. Mrk 509, Kaastra et al. 2012). Indeed the kinematics of the narrow emission lines, in terms of the velocity widths and a tentative indication of modest blueshift (both of the order of a few hundred $\mathrm{km\,s}^{-1}$), may imply we are observing emission from a pc scale outflow, but viewed out of the line of sight towards Ark 120.

7. Acknowledgements

REFERENCES

Anders, E., & Grevesse, N. 1989, Geochim. Cosmochim. Acta, 53, 197

Antonucci, R. 1993, ARA&A, 31, 473

Asplund, M., Grevesse, N., Sauval, A. J., & Scott, P. 2009, ARA&A, 47, 481

Baldwin, J., Ferland, G., Korista, K., & Verner, D. 1995, ApJ, 455, L119

Baumgartner, W. H., Tueller, J., Markwardt, C. B., et al. 2013, ApJS, 207, 19

Behar, E., Sako, M., & Kahn, S. M. 2001, ApJ, 563, 497

Blustin, A. J., Page, M. J., Fuerst, S. V., Branduardi–Raymont, G., & Ashton, C. E. 2005, A&A, 431, 111

Blustin, A. J., Branduardi-Raymont, G., Behar, E., et al. 2003, A&A, 403, 481

Braito, V., Reeves, J. N., Gofford, J., et al. 2014, ApJ, 795, 87

Braito, V., Reeves, J. N., Dewangan, G. C., et al. 2007, ApJ, 670, 978

Canizares, C. R., Davis, J. E., Dewey, D., et al. 2005, PASP, 117, 1144

Crenshaw, D. M., Kraemer, S. B., & George, I. M. 2003, ARA&A, 41, 117

Crenshaw, D. M., & Kraemer, S. B. 2001, ApJ, 562, L29

Crenshaw, D. M., Kraemer, S. B., Boggess, A., et al. 1999, ApJ, 516, 750

Davidson, K., & Netzer, H. 1979, Reviews of Modern Physics, 51, 715

den Herder, J. W., Brinkman, A. C., Kahn, S. M., et al. 2001, A&A, 365, L7

Detmers, R. G., Kaastra, J. S., Steenbrugge, K. C., et al. 2011, A&A, 534, 38

de Vries, C. P., den Herder, J. W., Kaastra, J. S., et al. 2003, A&A, 404, 959

Di Gesu, L., Costantini, E., Ebrero, J., et al. 2015, A&A, 579, A42

Done, C., Davis, S. W., Jin, C., Blaes, O., & Ward, M. 2012, MNRAS, 420, 1848

Emmanoulopoulos, D., Papadakis, I. E., McHardy, I. M., et al. 2011, MNRAS, 415, 1895

Eracleous, M., & Halpern, J. P. 2003, ApJ, 599, 886

Gaskell, C. M. 2009, New Astron., 53, 140

Gatuzz, E., García, J., Mendoza, C., et al. 2014, ApJ, 790, 131

Gofford, J., Reeves, J. N., Tombesi, F., et al. 2013, MNRAS, 430, 60

Gorczyca, T. W., Bautista, M. A., Hasoglu, M. F., et al. 2013, ApJ, 779, 78

Grevesse, N., & Sauval, A. J. 1998, Space Sci. Rev., 85, 161

Jin, C., Ward, M., & Done, C. 2012, MNRAS, 425, 907

Kaastra, J. S., Kriss, G. A., Cappi, M., et al. 2014, Science, 345, 64

Kaastra, J. S., Detmers, R. G., Mehdipour, M., et al. 2012, A&A, 539, A117

Kaastra, J. S., de Vries, C. P., Steenbrugge, K. C., et al. 2011, A&A, 534, A37

Kaastra, J. S., Mewe, R., Liedahl, D. A., Komossa, S., & Brinkman, A. C. 2000, A&A, 354, L83

Kalberla, P. M. W., Burton, W. B., Hartmann, D., et al. 2005, A&A, 440, 775

Kallman, T. R., Palmeri, P., Bautista, M. A., Mendoza, C., & Krolik, J. H. 2004, ApJS, 155, 675

Kaspi, S., Maoz, D., Netzer, H., et al. 2005, ApJ, 629, 61

Kaspi, S., Brandt, W. N., George, I. M., et al. 2002, ApJ, 574, 643

Kinkhabwala, A., Sako, M., Behar, E., et al. 2002, ApJ, 575, 732

Krolik, J. H., & Kriss, G. A. 2001, ApJ, 561, 684

Krolik, J. H., Horne, K., Kallman, T. R., et al. 1991, ApJ, 371, 541

Lamer, G., Uttley, P., & McHardy, I. M. 2003, MNRAS, 342, L41

Lobban, A. P., Reeves, J. N., Miller, L., et al. 2011, MNRAS, 414, 1965

Lodders, K. 2003, ApJ, 591, 1220

Lohfink, A. M., Reynolds, C. S., Miller, J. M., et al. 2012, ApJ, 758, 67

Longinotti, A. L., Krongold, Y., Kriss, G. A., et al. 2013, ApJ, 766, 104

Longinotti, A. L., Costantini, E., Petrucci, P. O., et al. 2010, A&A, 510, A92

Longinotti, A. L., Nucita, A., Santos-Lleo, M., & Guainazzi, M. 2008, A&A, 484, 311

Longinotti, A. L., Bianchi, S., Santos-Lleo, M., et al. 2007, A&A, 470, 73

Matt, G., Marinucci, A., Guainazzi, M., et al. 2014, MNRAS, 439, 3016

McKernan, B., Yaqoob, T., George, I. M., & Turner, T. J. 2003, ApJ, 593, 142

McKernan, B., Yaqoob, T., & Reynolds, C. S. 2007, MNRAS, 379, 1359

Mor, R., Netzer, H., & Elitzur, M. 2009, ApJ, 705, 298

Nardini, E., Fabian, A. C., Reis, R. C., & Walton, D. J. 2011, MNRAS, 410, 1251

Nordgren, T. E., Helou, G., Chengalur, J. N., Terzian, Y., & Khachikian, E. 1995, ApJS, 99, 461

Nucita, A. A., Guainazzi, M., Longinotti, A. L., et al. 2010, A&A, 515, A47

Ogle, P. M., Mason, K. O., Page, M. J., et al. 2004, ApJ, 606, 151

Osterbrock, D. E., & Phillips, M. M. 1977, PASP, 89, 251

Patrick, A. R., Reeves, J. N., Porquet, D., et al. 2011, MNRAS, 411, 2353

Peterson, B. M., Ferrarese, L., Gilbert, K. M., et al. 2004, ApJ, 613, 682

Peterson, B. M., & Gaskell, C. M. 1991, ApJ, 368, 152

Pinto, C., Kriss, G. A., Kaastra, J. S., et al. 2012, A&A, 541, A147

Pinto, C., Kaastra, J. S., Costantini, E., & Verbunt, F. 2010, A&A, 521, A79

Porquet, D., Dubau, J., & Grosso, N. 2010, Space Sci. Rev., 157, 103

Porquet, D., Reeves, J. N., O'Brien, P., & Brinkmann, W. 2004, A&A, 422, 85

Porquet, D., & Dubau, J. 2000, A&AS, 143, 495

Pounds, K. A., & Vaughan, S. 2011, MNRAS, 415, 2379

Reeves, J. N., Porquet, D., Braito, V., et al. 2013, ApJ, 776, 99

Reeves, J. N., Gofford, J., Braito, V., & Sambruna, R. 2010, ApJ, 725, 803

Reeves, J. N., Nandra, K., George, I. M., et al. 2004, ApJ, 602, 648

Reynolds, C. S. 1997, MNRAS, 286, 513

Risaliti, G., Bianchi, S., Matt, G., et al. 2005a, ApJ, 630, L129

Risaliti, G., Elvis, M., Fabbiano, G., Baldi, A., & Zezas, A. 2005b, ApJ, 623, L93

Sako, M., Kahn, S. M., Behar, E., et al. 2001, A&A, 365, L168

Stark, A. A., Gammie, C. F., Wilson, R. W., et al. 1992, ApJS, 79, 77

Sunyaev, R. A., & Titarchuk, L. G. 1985, A&A, 143, 374

Tatum, M. M., Turner, T. J., Sim, S. A., et al. 2012, ApJ, 752, 94

Terashima, Y., Gallo, L. C., Inoue, H., et al. 2009, PASJ, 61, S299

Theureau, G., Coudreau, N., Hallet, N., et al. 2005, A&A, 430, 373

Titarchuk, L. 1994, ApJ, 434, 570

Tombesi, F., Cappi, M., Reeves, J. N., et al. 2013, MNRAS, 430, 1102

Tombesi, F., Cappi, M., Reeves, J. N., et al. 2010, A&A, 521, A57

Turner, T. J., & Miller, L. 2009, A&A Rev., 17, 47

Turner, T. J., Reeves, J. N., Kraemer, S. B., & Miller, L. 2008, A&A, 483, 161

Vaughan, S., Fabian, A. C., Ballantyne, D. R., et al. 2004, MNRAS, 351, 193

Urry, C. M., & Padovani, P. 1995, PASP, 107, 803

Wandel, A., Peterson, B. M., & Malkan, M. A. 1999, ApJ, 526, 579

Willingale, R., Starling, R. L. C., Beardmore, A. P., Tanvir, N. R., & O'Brien, P. T. 2013, MNRAS, 431, 394

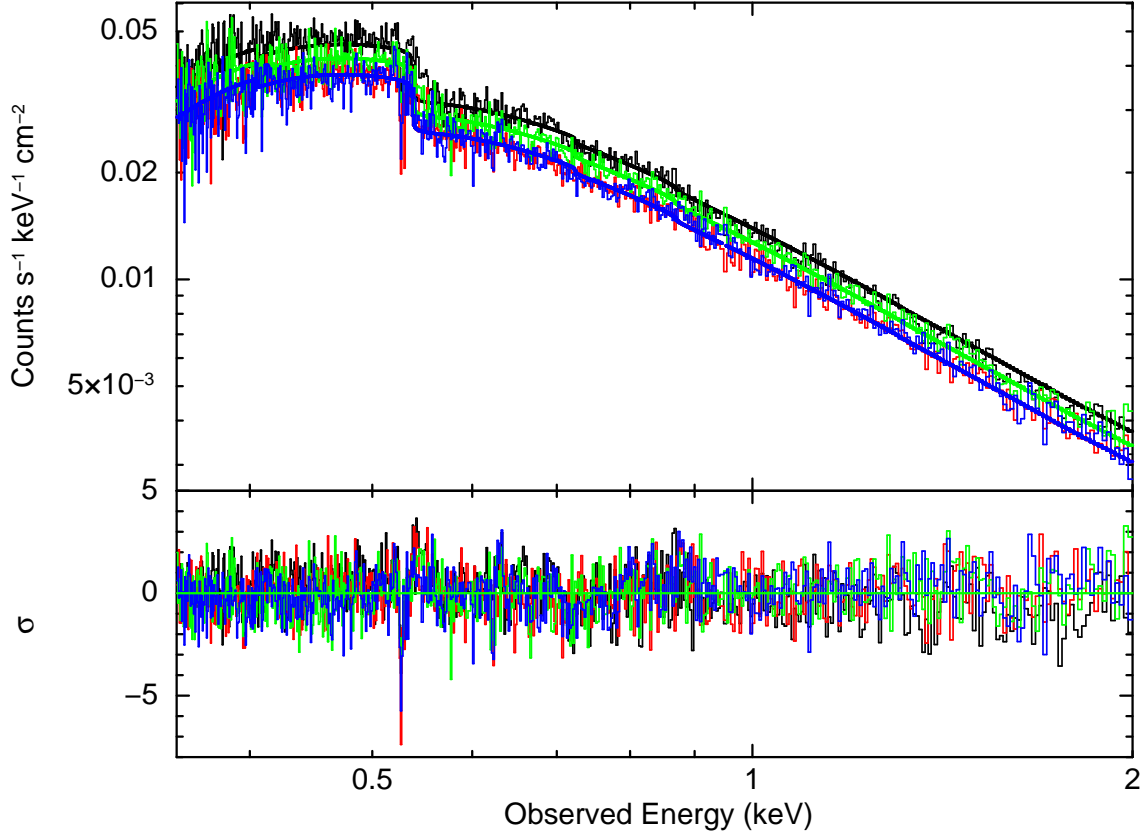Wilms, J., Allen, A., & McCray, R. 2000, ApJ, 542, 914

Fig. 1.— The upper panel shows the XMM-Newton RGS count rate spectra, divided by the instrumental effective area. The 4 individual RGS sequences in 2014 are plotted as histograms (in black, red, green and blue respectively). The baseline continuum model, as described in the text, is shown as a solid line. The lower panel show the residuals due to the model, the deviation seen near to 0.52 keV is due to bound-bound absorption from neutral O I due to our own Galaxy. Note all 4 RGS spectra are consistent with one another, except for a ±10% offset due to the different flux levels of each observation.
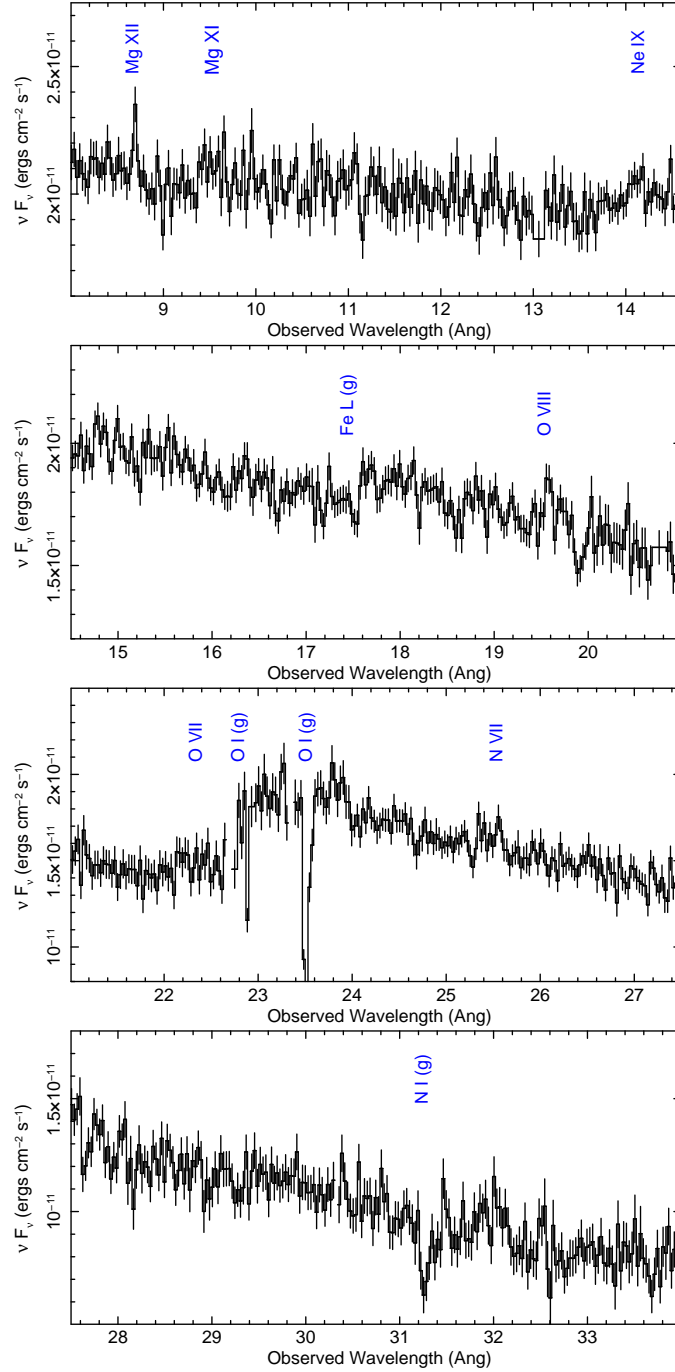
Fig. 2.— The four panels show the fluxed 2014 RGS spectrum of Ark 120, obtained from combining all 4 sequences and from the RGS 1 and RGS 2 data. The spectra have been fluxed against a power-law continuum of photon index $\Gamma = 2$ to create a νF_ν plot and are plotted against wavelength (in Angstroms) in the observed frame. The wavelengths of some of the expected emission lines from abundant elements are indicated, while the predicted position of absorption due to the ISM of our own Galaxy are also marked (denoted with a g symbol). Note the strong absorption lines and edge due to neutral O and N from our own Galaxy, as well as the possible presence due to photoionized emission lines from N, O, Ne and Mg in the rest-frame of Ark 120.
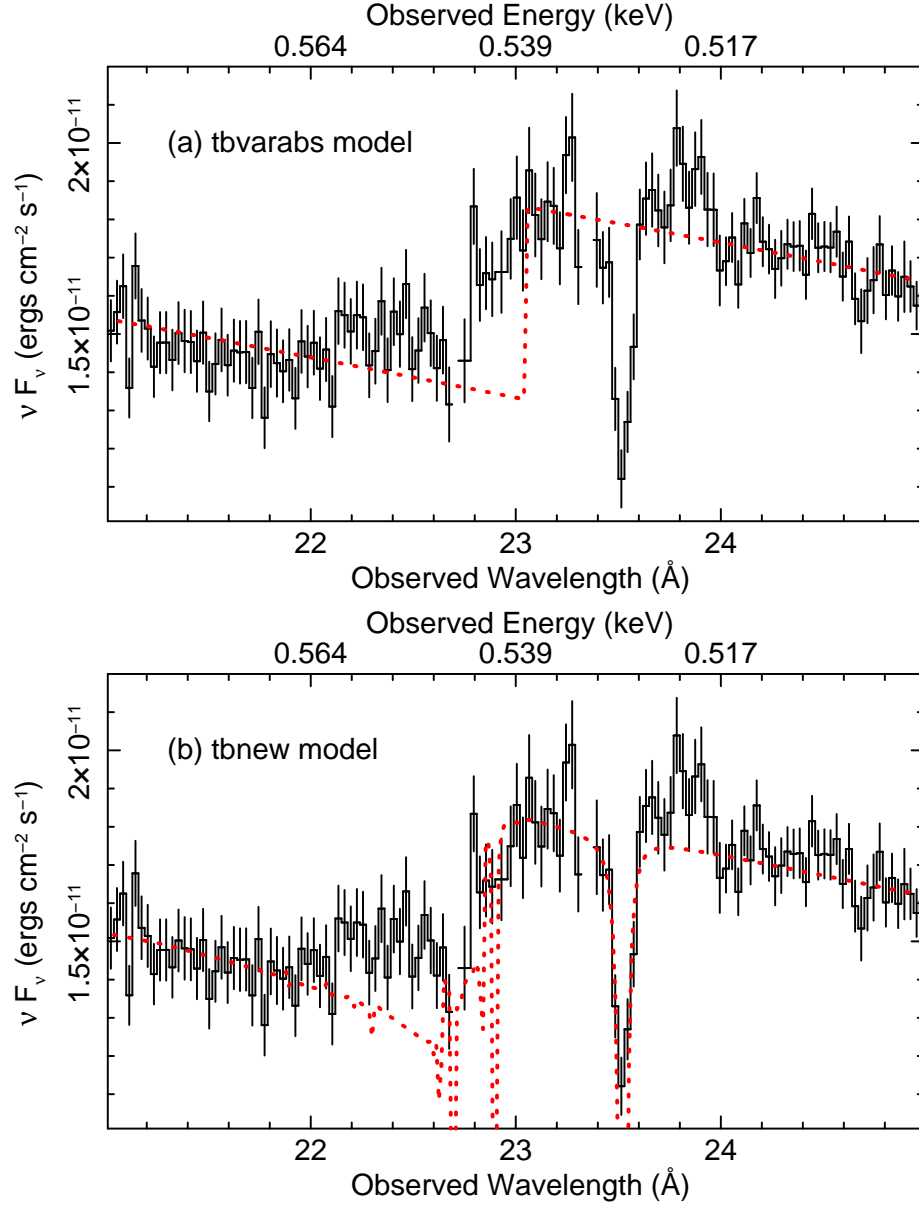
Fig. 3.— A zoom in of the fluxed RGS spectrum of Ark 120 in the neutral O K edge region, due to absorption in the Galactic ISM towards Ark 120. Wavelength (energy) is plotted in the observed ($z = 0$) frame. The top panel (a) shows the data compared against the TBVARABS absorption model (red dotted line), where a simple O I edge which is not able to correctly account for the absorption in this region. The lower panel (b) shows the comparison against the TBNEW model, which reproduces well the O I Kα absorption line at 23.5Å (or 527 eV), while the drop around the edge below 23Å is more gradual due to the higher order resonances present in the model. The excess blue-wards of the O edge is likely due to O VII emission associated with the AGN. Note that the models are superimposed on the spectra that have been fluxed against a $\Gamma = 2$ powerlaw, but the data are not unfolded against either absorption model.
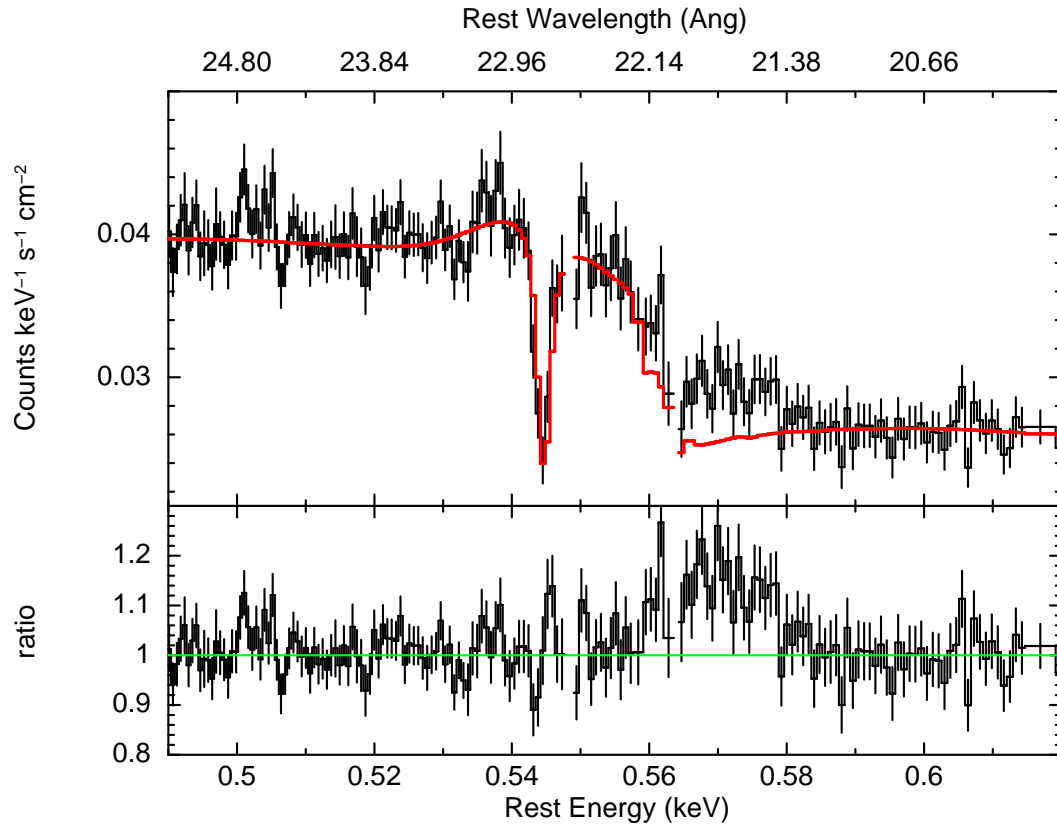
Fig. 4.— The RGS 1 count rate spectrum of Ark 120 in the O K-shell band. The TBNEW baseline absorption model as described in Figure 3 is shown in red, folded through the instrumental RGS response. Energy (wavelength on the upper-axis) is plotted in the AGN rest frame. A broad O VII emission line complex is apparent in the data/model ratio residuals observed by RGS 1, as observed in the 560-580 eV region, at energies above the neutral O K-shell absorption due to our Galaxy.
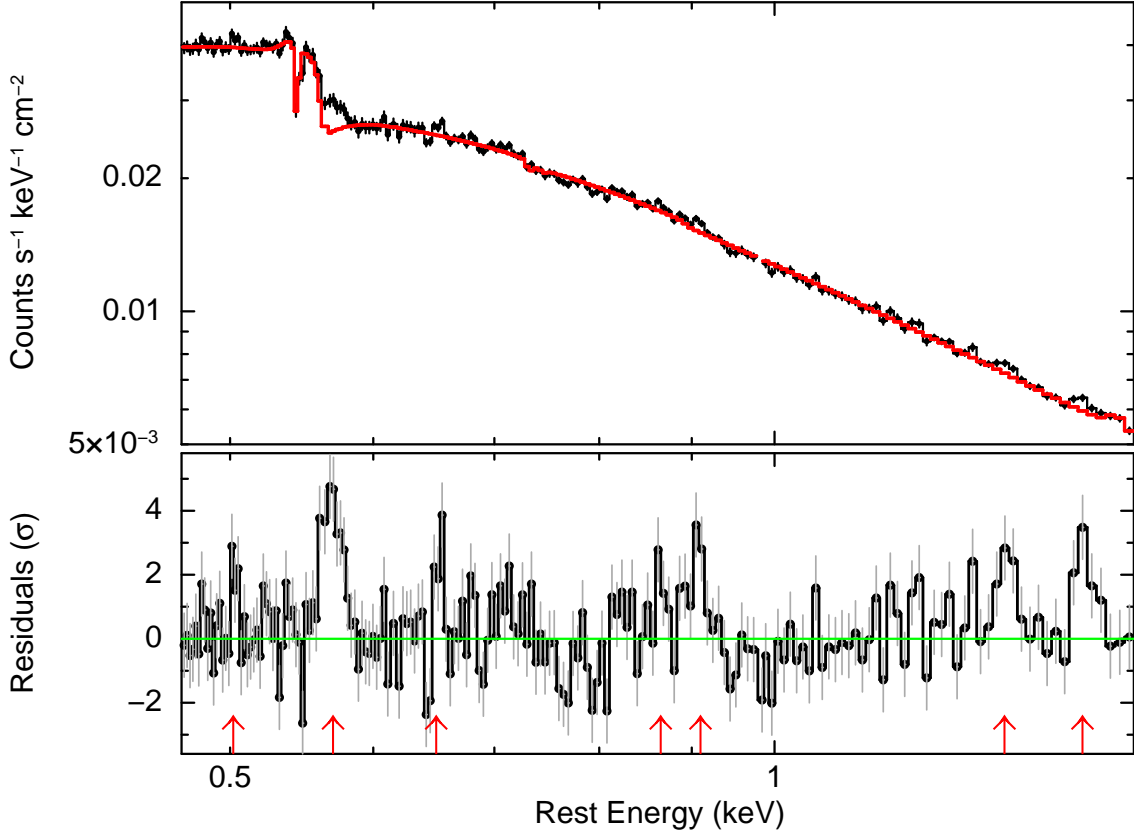
Fig. 5.— View of the RGS spectrum of Ark 120, plotted over the 0.4-1.6 keV rest energy band. For illustration, the spectrum has been more coarsely binned (compared to the instrumental resolution) to $\Delta\lambda = 0.1$Å per bin. The upper panel shows the data points as black points vs rest frame energy (in counts space), while the best fit TBNEW ISM absorption model (as listed in Table 2) is overlayed in red. Overall this model provides a good representation of the shape of the X-ray continuum in the RGS band. The lower panel shows the residuals (in σ units) of the data points compared to this model. Several positive deviations (at $> 3\sigma$ confidence) are marked along the x-axis by vertical arrows, which are observed at energies corresponding to 502 eV, 568 eV, 654 eV, 865 eV, 905 eV, 1343 eV and 1476 eV (to within ± 1 eV uncertainty). These may correspond to a series of emission lines, associated with the AGN, due to N VII Lyα, O VII Heα, O VIII Lyα, Fe XVIII $3d \rightarrow 2p$, Ne IX Heα, Mg XI Heα and Mg XII Lyα respectively.
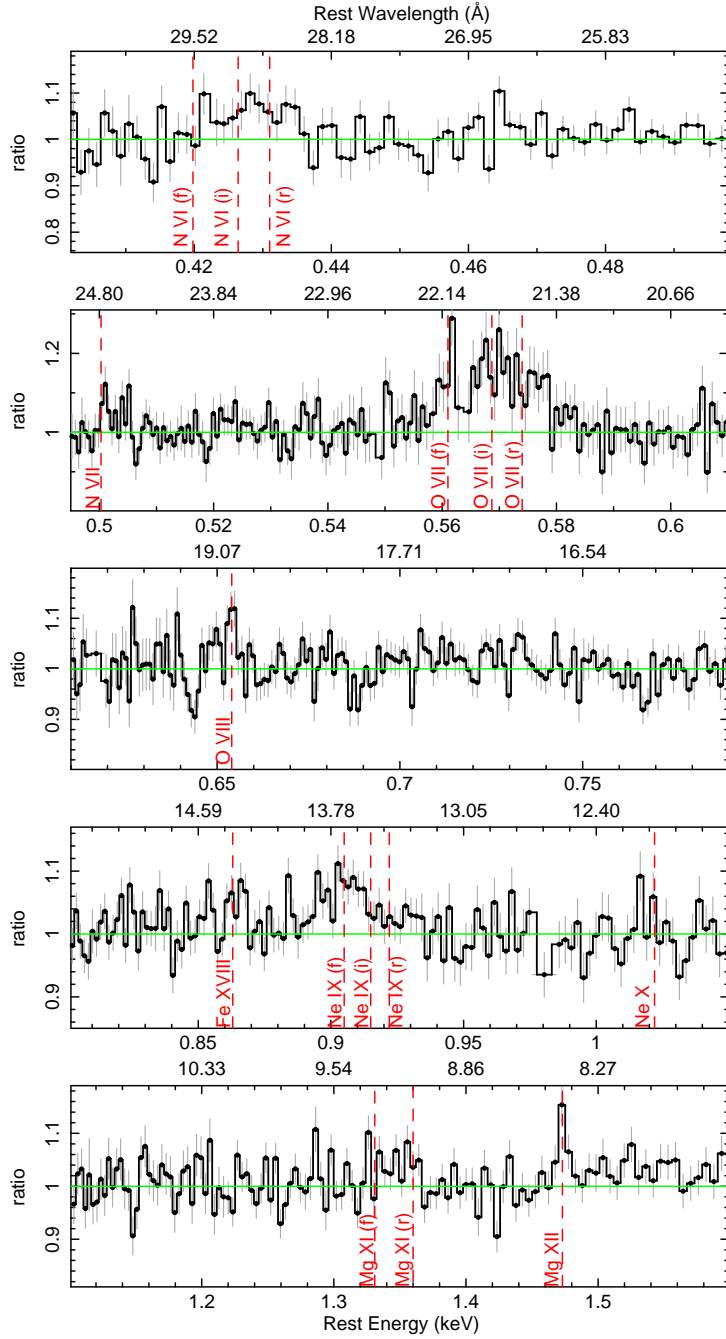
Fig. 6.— Data/Model ratio residuals of the RGS data to the best-fit ISM absorption model obtained with the baseline TBNEW model. Rest energy (in keV) is plotted along the low x-axis, rest wavelength (in Angstroms) along the upper axis. Dashed lines mark the expected positions of the strongest He-like (Heα) and H-like (Lyman-α) emission lines, where the He-like triplets are denoted by the forbidden (*f*), intercombination (*i*) and resonance (*r*) components respectively. The panels (from top to bottom) represent the residuals in the region of the N VI, O VII, O VIII, Ne IX–X and Mg XI–XII bands. Note the data are binned at the HWHM resolution of the RGS, except the upper-panel around N VI, which is binned by a further factor of ×3 for display only.
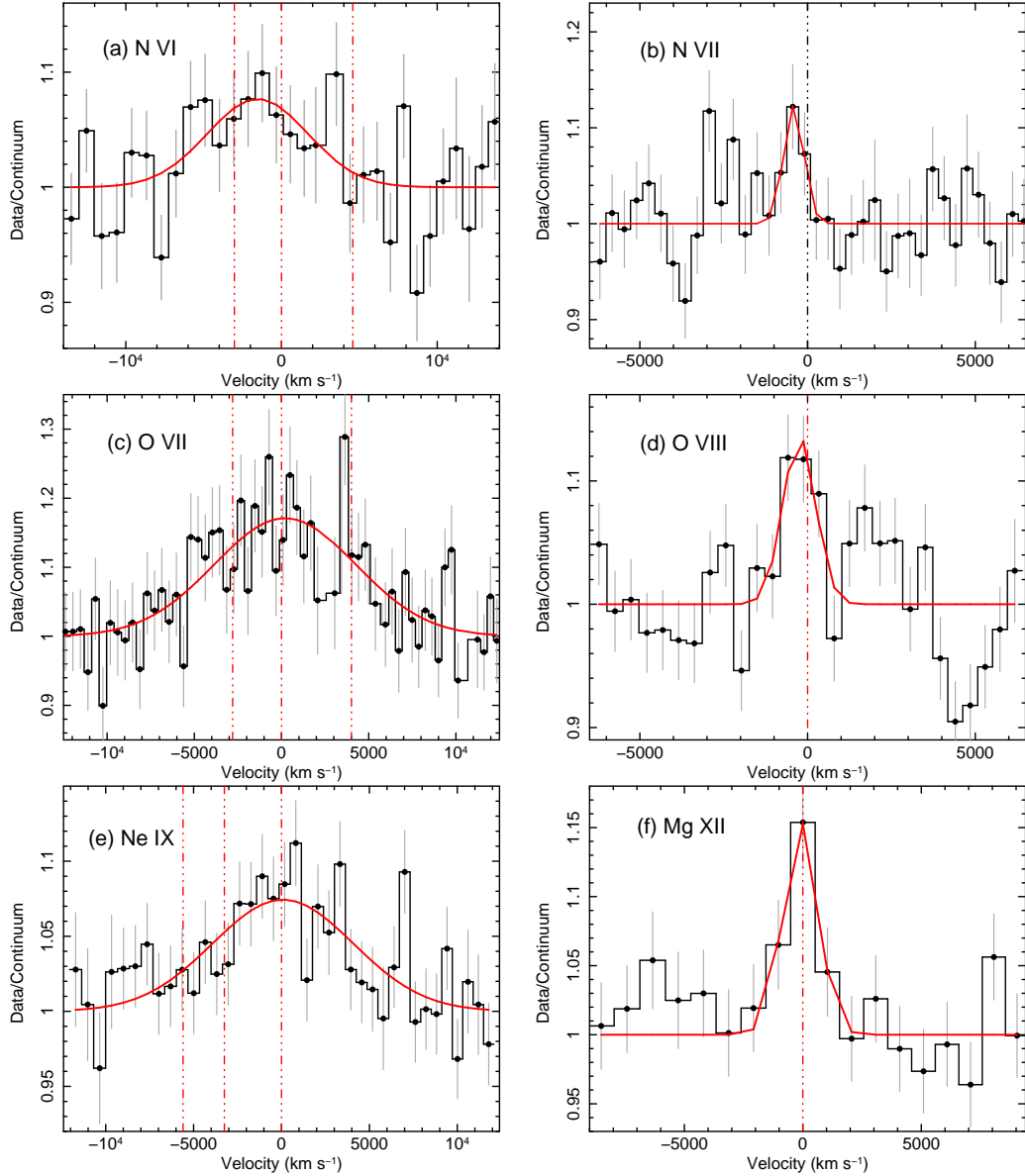
Fig. 7.— Velocity profiles of the main He and H-lines, as measured by XMM-Newton RGS for (a) N VI, (b) N VII, (c) O VII, (d) O VIII, (e) Ne IX and (f) Mg XII, see Section 5.2 for details. The points (filled circles) show the data divided by the continuum model for each line, where negative velocities correspond to blue-shifts. The profiles are centered at zero velocity, compared to the known line centroid energies of the doublets for H-like lines, the intercombination emission for N VII and O VII and the forbidden line for Ne IX. The solid line represents the best-fit single Gaussian emission profile for each line profile, with values reported in Table 5. In the case of the He-like emission (left hand panels), the profiles are all resolved and appear broadened, while the expected positions of the resonance, intercombination and forbidden components (left to right) are marked by vertical dot–dashed lines. In contrast, the H-like lines (right hand panels) appear unresolved, compared to the instrumental resolution.
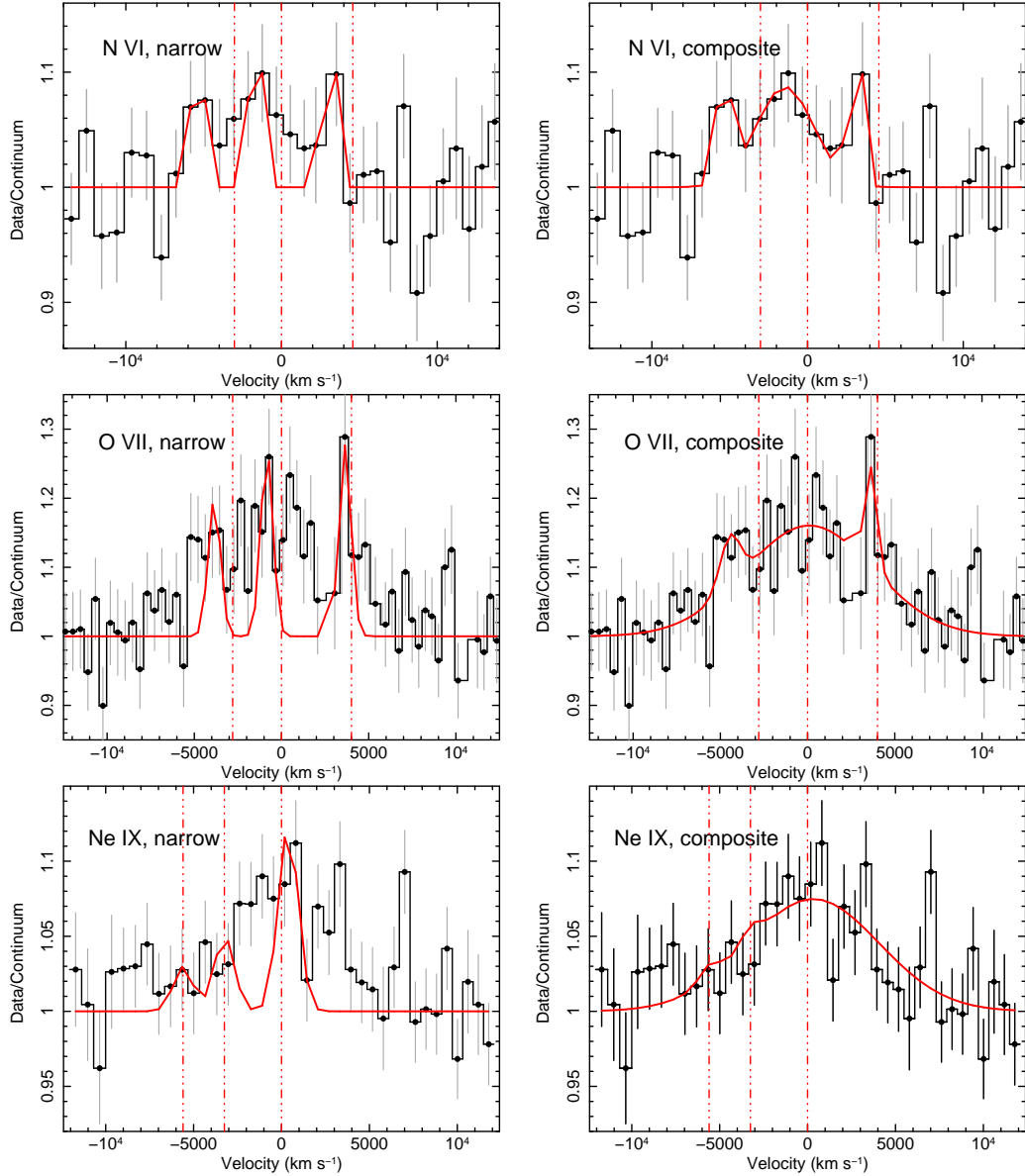
Fig. 8.— As per Figure 7, but showing the fits to the He-like profiles. The left hand panels are the fits to the profiles with a combination of three narrow, unresolved emission lines, corresponding to (from left to right) the resonance, intercombination and forbidden components and allowing for a small blue-shift of the lines where required. Overall, the three narrow triplet components provide a poor overall representation of the profiles, leaving significant remaining emission unmodeled. The right hand panels correspond to composite fits, where a broad emission component is included in the line profile, in addition to any narrow line emission where required. For the cases of O VII and Ne IX in particular, the profiles are dominated by an underlying broad (FWHM $\sim 8000\,\mathrm{km\,s^{-1}}$) line, corresponding to intercombination emission for O VII and forbidden emission for Ne IX, while any contributions from narrow components are small. The profiles indicate that most of the He-like line emission arises from denser gas, of the order $\sim 10^{11}\,\mathrm{cm^{-3}}$, with velocities commensurate with the AGN Broad Line Region.
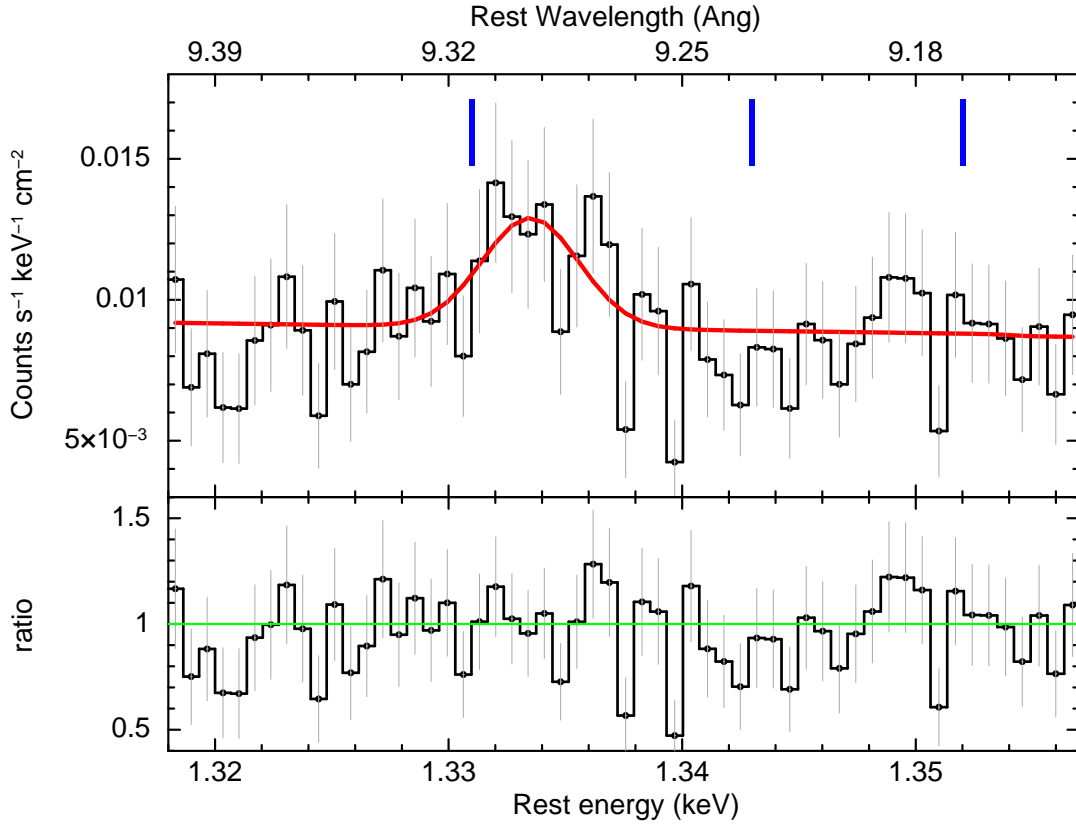
Fig. 9.— Portion of the Chandra HEG spectrum of Ark 120, in the region of the Mg XI He-like triplet, plotted in the AGN rest frame. The expected positions (from left to right) of the forbidden, intercombination and resonance line components are marked with blue vertical lines. Significant line emission is detected just bluewards of the expected position of the forbidden line, while no emission is required from either of the intercombination or resonance components. Due to the high resolution of the HEG spectrum, the forbidden line is resolved, with a width of $\sigma_v = 450^{+290}_{-180} \, \mathrm{km \, s^{-1}}$ and likely corresponds to the narrow component of emission which is unresolved in the RGS. Note that the spectral bins sample the HWHM resolution of the HEG, which corresponds to $\Delta\lambda = 0.005\text{Å}$ or $\sim 160 \, \mathrm{km \, s^{-1}}$ at the position of the Mg XI triplet.
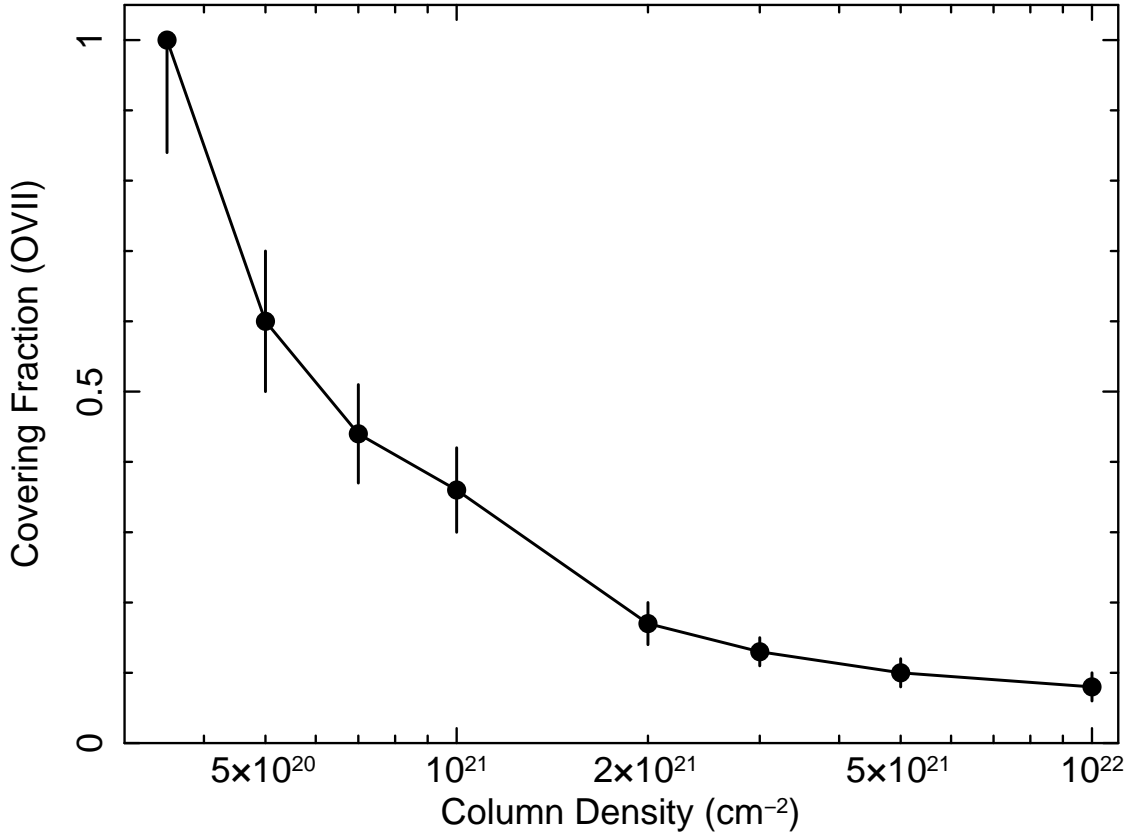
Fig. 10.— Geometric covering fraction (as a fraction of 4π steradian) of the broad line soft X-ray emitting gas responsible for the broad O VII profile. This has been fitted as a function of the emitter column density, from the photoionized emission model discussed in Section 6.4. The covering fraction for the O VII gas decreases with column density, with a minimum covering fraction of $f = 0.1$ (i.e. 10% of 4π steradian) deduced for columns of $N_{\rm H} = 10^{22}$ cm^{-2} and higher. A minimum column density of $N_{\rm H} > 3\times10^{20}$ cm^{-2} is required corresponding to where the gas fully covers the AGN with $f = 1$. Overall the deduced parameters appear consistent with the expected gas distribution in the AGN Broad Line Region.

Table 1.   Summary of Ark 120 Observations

Mission	Obsid	Start Date/Time[a]	Inst	Exposure (ks)	Net Rate s^{-1}
XMM-Newton	0721600201	2014-03-18 08:52:49	RGS 1	108.8	0.795 ± 0.003
	–	–	RGS 2	–	0.909 ± 0.003
	0721600301	2014-03-20 08:58:47	RGS 1	116.6	0.653 ± 0.003
	–	–	RGS 2	–	0.747 ± 0.003
	0721600401	2014-03-22 08:25:17	RGS 1	102.8	0.718 ± 0.003
	–	–	RGS 2	–	0.831 ± 0.003
	0721600501	2014-03-24 08:17:19	RGS 1	103.6	0.654 ± 0.003
	–	–	RGS 2	–	0.746 ± 0.003
	Total	–	RGS 1	431.9[b]	0.705 ± 0.001
		–	RGS 2	430.8[b]	0.808 ± 0.001
		–	RGS 1+2	862.7[b]	0.756 ± 0.001
Chandra	16539	2014-03-17 07:47:58	MEG	63.0	0.914 ± 0.004
	–	–	HEG	–	0.417 ± 0.003
	15636	2014-03-21 04:38:43	MEG	10.2	0.752 ± 0.011
	–	–	HEG	–	0.356 ± 0.009
	16540	2014-03-22 13:55:12	MEG	47.3	0.832 ± 0.005
	–	–	HEG	–	0.389 ± 0.004
	Total	–	MEG	120.5	0.868 ± 0.003
	–	–	HEG	–	0.401 ± 0.002

[a]Observation Start/End times are in UT.

[b]Net exposure time, after screening and deadtime correction, in ks.

Table 2.   Baseline Model Parameters to 2014 Ark 120 RGS Spectrum

Component	Parameter	Value
Continuum:-		
Galactic absorption	$N_{\mathrm{H}}{}^{a}$	8.8 ± 0.4
	$A_O{}^{b}$	1.62 ± 0.10
Powerlaw	Γ	2.06 ± 0.06
	$N_{\mathrm{PL}}{}^{c}$	1.38 ± 0.04
Blackbody	kT^{d}	126 ± 6
	N_{BB}^{e}	9.7 ± 1.7
Absorption Lines:-		
N I Kα^{g}	$E_{\mathrm{obs}}\ (\lambda_{\mathrm{obs}})$	396.6 ± 0.5 [31.26]
	N_{ph}	-7.2 ± 0.7
	EW	0.59 ± 0.06
O I Kα^{g}	$E_{\mathrm{obs}}\ (\lambda_{\mathrm{obs}})$	527.2 ± 0.2 [23.52]
	N_{ph}	-7.0 ± 1.0
	EW	1.14 ± 0.16
Flux	$F_{0.4-2.0}{}^{h}$	2.95

[a]Galactic neutral absorption column, modeled with tb-new, units $\times 10^{20}\,\mathrm{cm}^{-2}$.

[b]O abundance, compared to the Solar abundance table of Wilms et al. (2000).

[c]Power law photon flux at 1 keV, in units of $\times 10^{-2}\,\mathrm{photons\,cm}^{-2}\,\mathrm{s}^{-1}\,\mathrm{keV}^{-1}$.

[d]Blackbody temperature, units eV.

[e]Blackbody normalization, in units of $\times 10^{-5}\frac{L_{39}}{D_{10\mathrm{kpc}}^{2}}$, where L_{39} is the luminosity in units of $\times 10^{39}\,\mathrm{erg\,s}^{-1}$ and $D_{10\mathrm{kpc}}$ is the source distance in units of 10 kpc.

[g]N I and O I Kα absorption line parameters. Energy (E_{obs}) (or wavelength λ_{obs} in brackets) are given in the observed ($z = 0$) frame in units of eV (or Å); photon flux (N_{ph}) is in units of $\times 10^{-5}\,\mathrm{photons\,cm}^{-2}\,\mathrm{s}^{-1}$; equivalent width (EW) is in units of eV.

[h]Observed (absorbed) continuum flux from 0.4–2.0 keV in units of $\times 10^{-11}\,\mathrm{erg\,cm}^{-2}\,\mathrm{s}^{-1}$.

Table 3.   Galactic ISM Absorption towards Ark 120.

Parameter	TBVARABS[a]	TBNEW[a]	ISMABS[a]	TBNEW[2a]	ISMABS[2a]
N_H[b]	9.4 ± 0.4	8.8 ± 0.4	8.51 ± 0.4	11.1 ± 0.4	11.4 ± 0.6
N_O[c]	6.4 ± 0.5	7.0 ± 0.5	6.5 ± 0.3	6.5 ± 0.3	6.1 ± 0.3
O/H[d]	6.8 ± 0.5	7.9 ± 0.5	7.7 ± 0.5	5.9 ± 0.3	5.4 ± 0.4
A_O[e]	1.39 ± 0.10	1.62 ± 0.10	1.57 ± 0.10	1.20 ± 0.04	1.10 ± 0.08
N_N[f]	–	–	0.72 ± 0.27	–	0.76 ± 0.25
N/H[g]	–	–	8.5 ± 3.2	–	6.7 ± 2.2
N_Ne[f]	–	–	1.2 ± 0.3	–	1.4 ± 0.3
Ne/H[g]	–	–	14 ± 4	–	12 ± 3
N_Fe[f]	–	–	0.26 ± 0.06	–	0.25 ± 0.05
Fe/H[g]	–	–	3.0 ± 0.7	–	2.2 ± 0.5
N_{O^+}[h]	–	–	< 0.42	–	–
$N_{\mathrm{O}^{2+}}$[h]	–	–	< 0.06	–	–
χ^2/dof	1392.7/934	1087.3/914	1086.6/911	1110.8/914	1093.6/911

[a]Galactic ISM absorption model, fitted with either TBVARABS, TBNEW or ISMABS. In the first three cases, the continuum is fitted with a power-law plus blackbody model to the RGS band, while in the latter TBNEW^2 and ISMABS^2 cases, the continuum is fitted with a power-law plus Comptonized blackbody spectrum.

[b]Galactic neutral hydrogen column, in units $\times 10^{20}\,\mathrm{cm}^{-2}$.

[c]Neutral Oxygen column, units $\times 10^{17}\,\mathrm{cm}^{-2}$.

[d]Derived ratio of O to H column density, $\times 10^{-4}$.

[e]Relative O/H abundance, compared to the Solar abundance value of 4.9×10^{-4} in Wilms et al. (2000).

[f]Column density of neutral N, Ne or Fe, in units $\times 10^{17}\,\mathrm{cm}^{-2}$.

[g]Derived ratio of N/H, Ne/H and Fe/H column densities, $\times 10^{-5}$. Note the relative Solar abundances listed in Wilms et al. (2000) are 7.6×10^{-5}, 8.71×10^{-5} and 2.69×10^{-5} for N/H, Ne/H and Fe/H respectively.

[h]Column density of once and twice ionized O towards Ark 120, in units $\times 10^{17}\,\mathrm{cm}^{-2}$.

Table 4.   Soft X-ray Emission Lines in the 2014 Ark 120 Spectrum

Line ID	E^a_{quasar}	Flux^b	EW^c	σ^d	$\Delta\chi^{2e}$
N VI (i)	428.4 ± 2.3 [28.941]	$9.6^{+4.5}_{-3.2}$	$0.83^{+0.39}_{-0.27}$	$4.9^{+1.9}_{-2.1}$	19.7
N VII Ly-α	501.0 ± 0.4 [24.747]	1.8 ± 0.5	0.23 ± 0.10	< 0.9	13.1
O VII (i)	$568.2^{+1.7}_{-1.6}$ [21.820]	$18.8^{+3.3}_{-3.0}$	2.8 ± 0.5	$6.8^{+1.5}_{-1.2}$	104.8
O VII (f)	561.0^f [22.100]	2.6 ± 2.2	0.4 ± 0.3	1^f	–
O VIII Ly-α	654.1 ± 0.5 [18.955]	2.1 ± 0.7	0.47 ± 0.16	< 1.1	27.2
Fe XVIII	864.7 ± 1.9 [14.338]	1.4 ± 0.6	0.60 ± 0.25	$2.1^{+2.3}_{-1.5}$	15.4
Ne IX (f)	904.8 ± 3.6 [13.703]	2.9 ± 0.8	1.4 ± 0.4	$7.1^{+4.4}_{-2.7}$	36.6
Mg XI	1342 ± 10 [9.239]	$1.6^{+0.9}_{-0.6}$	$1.9^{+1.1}_{-0.7}$	< 24	16.7
Mg XI^g (f)	$1333.5^{+1.3}_{-1.5}$ [9.297]	2.4 ± 1.1	2.2 ± 1.0	$2.0^{+1.3}_{-0.8}$	14.8
Mg XII	1475^{+1}_{-3} [8.406]	1.8 ± 0.6	2.6 ± 0.9	< 3.6	28.1

^{a}Measured line energy in quasar rest frame, units eV. The corresponding rest wavelength value in Å is given within brackets. Note the lines are measured with the RGS, unless otherwise stated.

^{b}Photon flux of line, units $\times 10^{-5}$ photons cm^{-2} s^{-1}

^{c}Equivalent width in quasar rest frame, units eV.

^{d}1σ velocity width, eV.

^{e}Improvement in $\Delta\chi^2$ (or ΔC for the HETG) upon adding line to model.

^{f}Indicates parameter is fixed.

^{g}Parameters measured from the Chandra HETG spectrum

Table 5. Fits to Velocity Profiles of Soft X-ray Emission Lines

Line ID	σ_v[a]	FWHM[a]	v_out[b]	Flux[c]
Single Gaussians[d]:-				
N VI He-α	3200 ± 1300	7500 ± 3000	-1500 ± 1000	$9.6^{+4.5}_{-3.2}$
N VII Ly-α	< 290	< 680	-410 ± 120	1.8 ± 0.5
O VII He-α	4050 ± 700	9500 ± 1600	< 730	$18.8^{+3.3}_{-3.0}$
O VIII Ly-α	< 470	< 1100	-250 ± 130	2.1 ± 0.7
Ne IX He-α	3980 ± 1100	9350 ± 2600	< 710	2.9 ± 0.8
Mg XI He-α[g] (f)	450^{+290}_{-180}	1050^{+680}_{-420}	-540^{+340}_{-290}	2.4 ± 1.1
Mg XII Ly-α	< 700	< 1650	< 300	1.8 ± 0.6
Three Gaussian fit[e]:-				
N VI triplet:-				
(f)	–	–	-1650 ± 400	< 3.6
(i)	1840 ± 820	4300 ± 1900	-1450 ± 700	6.3 ± 3.0
(r)	–	–	< 2300	< 2.5
O VII triplet:-				
(f)	–	–		6.9 ± 2.8
(i)	2000^{+1200}_{-800}	4600^{+2700}_{-2000}	< 850	6.5 ± 2.5
(r)	–	–		6.4 ± 2.3
Ne IX triplet:-				
(f)	2300^{+1800}_{-1100}	5500^{+4200}_{-2600}	< 930	3.0 ± 1.1
(i)	–	–	–	< 0.6
(r)	–	–	–	< 0.5

[a]Intrinsic 1σ and FWHM velocity widths of emission lines in $\mathrm{km\,s^{-1}}$, after correcting (in quadrature) for instrumental spectral resolution.

[b]Velocity shift of emission line in $\mathrm{km\,s^{-1}}$. Negative values denote blue-shift. The velocity centroids of the N VI and O VII lines are measured with respect to the inter-combination emission and Ne IX is with respect to the forbidden line.

[c]Flux of the individual He-like line components, in units $\times 10^{-5} \, \mathrm{photons\,cm^{-2}\,s^{-1}}$.

[d]Profile fitted with a single Gaussian component only.

[e]He-like profiles fitted with a blend of three broad Gaussian lines, with a common velocity width between the three components. Note f, i and r denote forbidden, inter-combination and resonance components respectively.

[g]Profile measured from the Chandra HETG spectrum

Table 6.   Soft X-ray emission zones modeled by XSTAR.

Zone	$\log \xi^a$	F_{cov} ($N_{\mathrm{H}} = 10^{21}\,\mathrm{cm}^{-2}$)^b	F_{cov} ($N_{\mathrm{H}} = 10^{22}\,\mathrm{cm}^{-2}$)^b
Broad (O VII)	0.5 ± 0.1	0.36 ± 0.06	0.08 ± 0.02
Broad (Ne IX)	1.5 ± 0.3	> 0.64	0.09 ± 0.03
Narrow (O VIII)	2.3 ± 0.4	> 0.62	0.11 ± 0.04

[a]Ionization parameter. Units of ξ are $\mathrm{erg\,cm\,s}^{-1}$ in log units.

[b]Covering fractions for column densities of $N_{\mathrm{H}} = 10^{21}\,\mathrm{cm}^{-2}$ and $10^{22}\,\mathrm{cm}^{-2}$ respectively.